

Multi-Scale Texture Loss for CT Denoising with GANs

Francesco Di Feola^{a,*}, Lorenzo Tronchin^b, Valerio Guarrasi^b, Paolo Soda^{a,b}

^a*Department of Diagnostics and Intervention, Radiation Physics, Biomedical Engineering, Umeå University, Sweden*

^b*Unit of Computer Systems and Bioinformatics, Department of Engineering, University Campus Bio-Medico of Rome, Italy*

Abstract

Generative Adversarial Networks (GANs) have proved as a powerful framework for denoising applications in medical imaging. However, GAN-based denoising algorithms still suffer from limitations in capturing complex relationships within the images. In this regard, the loss function plays a crucial role in guiding the image generation process, encompassing how much a synthetic image differs from a real image. To grasp highly complex and non-linear textural relationships in the training process, this work presents a loss function that leverages the intrinsic multi-scale nature of the Gray-Level-Co-occurrence Matrix (GLCM). Although the recent advances in deep learning have demonstrated superior performance in classification and detection tasks, we hypothesize that its information content can be valuable when integrated into GANs' training. To this end, we propose a differentiable implementation of the GLCM suited for gradient-based optimization. Our approach also introduces a self-attention layer that dynamically aggregates the multi-scale texture information extracted from the images. We validate our approach by carrying out extensive experiments in the context of low-dose CT denoising, a challenging application that aims to enhance the quality of noisy CT scans. We utilize three publicly available datasets, including one simulated and two real datasets. The results are promising as compared to other well-established loss functions, being also consistent across three different GAN architectures. The code is available at: <https://github.com/FrancescoDiFeola/DenoTextureLoss>

Keywords: Low-dose CT (LDCT), deep learning, noise reduction, image translation, Generative Adversarial Networks, image synthesis

1. Introduction

Medical imaging provides a powerful non-invasive visualization tool to reveal details about the internal human body structures. However, due to the non-idealities of the imaging processes, medical images often contain noise and

*Corresponding author: email: francesco.feola@umu.se;

artifacts, reducing the chance for an accurate diagnosis. Therefore, image denoising has become a crucial step in preprocessing medical images (Burgos and Svoboda (2022)), involving the inspection of a noisy image and the restoration of an approximation of the underlying clean counterpart (Izadi et al. (2023)). Among different imaging modalities, Computed Tomography (CT) is of particular interest in the field of denoising. Basing its functioning on the absorption of X-rays, it has been proved that ionizing radiation can cause damage at different levels in biological material (Brenner and Hall (2007)). Due to this evidence, much effort has been put into reducing and optimizing radiation exposure under the ALARA (As Low As Reasonably Achievable) principle (Bevelacqua (2010)). With the increasing use of CT in many clinical applications, screenings included, the use of Low-Dose (LD) acquisition protocols has become a clinical practice (Ohno et al. (2019)) preferred over High-Dose (HD) protocols. However, if on the one side, it reduces the dose delivered to patients, on the other side, the overall quality of the reconstructed CT decreases. This motivates the investigation of image-denoising strategies that aim to obtain high-quality CT images at the lowest cost in terms of radiation.

Traditional approaches for image denoising impose explicit regularization, leveraging a priori knowledge about the noise distribution, and building a relation between relevant information and the noise present in the images. Some examples include dictionary learning approaches (Aharon et al. (2006)) and non-local means filtering (Dabov et al. (2007)). These methods typically lack generalization, being able to perform well only under specific assumptions and specific hyperparameters. The advent of Deep Learning (DL) has paved the way for improved generalization capacity in denoising algorithms. Not needing any assumptions, DL approaches automatically learn useful features while training in an end-to-end manner, accommodating different kinds of data and they can roughly be divided into paired and unpaired methods. The former make use of paired datasets, i.e., they need the LD images and their respective HD counterparts, performing supervised training. The need for paired datasets represents a strong limitation for the actual application of these algorithms. Indeed, the collection of coupled datasets is not only expensive and time-consuming, but is also unfeasible from a clinical perspective on a large scale (Li et al. (2020b)), where efforts are made to reduce the number of examinations to the patient as much as possible. Due to the intrinsic unpaired nature of the existing datasets, *unpaired deep-learning methods* are the most suitable to address CT image denoising.

Among denoising approaches, the use of Generative Adversarial Networks (GANs) is a promising approach, being successfully employed for a variety of image-to-image translation tasks (Pang et al. (2021)). The backbone of a GAN consists of a generator and a discriminator network. The generator learns to produce samples that fit the data distribution of the target domain while the discriminator acts as a classifier of the generated samples, attempting to distinguish between real samples and fake samples produced by the generator. In LDCT denoising, the generator is tasked with generating realistic denoised images, whilst the discriminator is designed to differentiate between denoised images from the HDCT counterparts. The most used backbones are Pix2Pix (Isola et al. (2017))

and CycleGAN (Zhu et al. (2017)). The former requires pairs of images in the training phase, restricting its application to paired datasets, whilst the latter relaxes this constraint with the introduction of cycle consistency, establishing itself as the milestone architecture for unpaired approaches.

To date, a variety of works have tackled paired and unpaired LDCT denoising with GANs either modifying the baseline model architecture or introducing novel loss functions. Indeed, as pointed out by Huang et al. (Huang et al. (2021)), the loss function’s role is crucial, even with a more substantial impact on denoising performance than the model architecture. While several authors used the L_2 norm (Wolterink et al. (2017); You et al. (2018); Du et al. (2019); Park et al. (2019); Han et al. (2021); Yin et al. (2021); Han et al. (2022); Yang et al. (2023); Bera and Biswas (2023)), also called Mean Squared Error (MSE), it is known that such a metric produces blurred images and poorly correlate with the visual perception of the image quality (Huang et al. (2021); Wang et al. (2004)). To overcome these limitations, L_1 norm is often employed as a valid alternative (Ma et al. (2020); Huang et al. (2021); Kwon and Ye (2021); Park et al. (2022); Li et al. (2023)), but it still minimizes per-pixel errors, thus neglecting spatial and anatomical relationships between pixels. This is why the integration of structural and semantic information into the loss function is highly recommended (Elad et al. (2023)).

To this end, although there exists a variety of loss functions proposed in the literature (Izadi et al. (2023); Zhao et al. (2016)), those based on deep perceptual similarity (Yang et al. (2018); Du et al. (2019); Li et al. (2020a); Yin et al. (2021); Gajera et al. (2021); Marcos et al. (2021); Li et al. (2021); Han et al. (2021, 2022); Li et al. (2022); Yin et al. (2023)), structural similarity (You et al. (2018); Ma et al. (2020); Li et al. (2021, 2023)), and Charbonnier distance (Gajera et al. (2021); Kyung et al. (2022); Li et al. (2022); Kang et al. (2023)) have been adopted to a larger extent in LDCT denoising (Kaur and Dong (2023)). Their rationale is now summarized and they are formally presented in section (3.1). Straightforwardly, the interested readers will find in the literature several works each one presenting a specific loss function, but their review is out of the scope of this manuscript and they can refer to recent surveys, e.g., (Pan et al. (2020); Kaur and Dong (2023)). Loss functions based on deep perceptual similarity extract feature maps from a pre-trained Convolutional Neural Network (CNN) (Gatys et al. (2015)): rather than matching pixel intensities, they minimize the distance between such deep features between the input and the corresponding synthetic image. The underlying assumption is that the similarity between deep features may indicate the degree of perceptual similarity between the images they come from. However, the reliability of deep features in terms of their perceptual or semantic meaning can be questioned as pointed out by Matsoukas et al. (2022): deep learning models encourage the reuse of learned representations that are not necessarily associated with semantic meaning, especially when using feature extractors pre-trained on ImageNet (Russakovsky et al. (2015)) applied to medical domains. The structural similarity is an alternative to L_1 and L_2 distances (Elad et al. (2023)): based on the assumption that human visual perception is highly adapted for extracting

structural information from a scene, it computes the local similarity between two images as a function of luminance, contrast, and structure to assess the degradation of structural information (Wang et al. (2004)). The Charbonnier distance is a smooth approximation of the Huber loss (Charbonnier et al. (1994); Gajera et al. (2021); Li et al. (2022); Kang et al. (2023)) that is quadratic for small variations and approximates the L_1 distance for large variations. On these grounds, we therefore believe that the definition of effective loss functions for image denoising is still an open challenge that deserves further investigation.

In the context of GAN-based LDCT denoising, we hereby introduce a Multi-Scale Texture Loss Function (MSTLF) that reinforces the models’ ability to learn complex relationships by extracting texture information at different scales. To this end, it leverages the intrinsic multiscale nature of the Gray-Level-Cooccurrence Matrix (GLCM). Essentially the GLCM is a handcrafted histogramming operation that counts how often different combinations of pixel intensity values occur in a specific spatial and angular relationship within an image. It is a powerful tool used for texture analysis in several fields, including medical imaging: it quantifies texture patterns and structure measuring smoothness, coarseness, and regularity (Depeursinge et al. (2017); Santucci et al. (2021)), i.e., all properties that characterize an image undergoing denoising. Although the recent advances in DL have outperformed its use for classification and detection tasks, our hypothesis is that its information content can still be valuable when integrated within DL models’ training. To the best of our knowledge, no one has ever tried to integrate the GLCM in a DL framework. Noticing it is non-differentiable, which makes it incompatible with gradient-based optimization, we propose a novel GLCM implementation that overcomes this limitation. Furthermore, with our proposed MSTLF, the process of embedding handcrafted descriptors within a deep learning framework is fully enabled by the use of a self-attention mechanism that provides for the dynamic end-to-end aggregation of the multiscale information. Experimental results on three publicly available datasets show that our approach outperforms standard loss functions and proves to be effective on different state-of-the-art GAN architectures.

Overall, our contributions can be summarized as follows:

- We propose a novel MSTLF that leverages texture descriptors extracted at different spatial and angular scales, effectively exploiting and embedding textural information into GAN-based denoising algorithms.
- Given the multi-scale nature of our approach, we introduce a novel aggregation rule based on self-attention that can effectively and dynamically merge multiscale texture information.
- We propose a novel implementation of the GLCM based on a soft assignment that makes the GLCM differentiable and compatible with gradient-based optimization.
- We perform extensive experimentation to prove the effectiveness of the proposed approach in both paired and unpaired scenarios, testing our models on three datasets, containing both real and simulated LDCT.

- We test our approach on three different GAN-based architectures, which bring out its agnostic behavior to the backbone used.

The rest of the paper is organized as follows: section 2 presents the methods, section 3 describes the experimental configuration, section 4 presents and discusses the results, whereas section 5 offers concluding remarks.

2. Methods

Let \mathbf{x} be a noisy image and \mathbf{y} the corresponding noise-free counterpart. The corruption by noise can be expressed as:

$$\mathbf{x} = \phi(\mathbf{y}) \quad (1)$$

where ϕ denotes a generic unknown degradation function. Image denoising aims to recover \mathbf{y} from \mathbf{x} by approximating the inverse function ϕ^{-1} that maps the noisy input \mathbf{x} to its clean counterpart $\hat{\mathbf{y}} = \phi^{-1}(\mathbf{x}) \approx \mathbf{y}$.

Our MSTLF approach for GAN-based denoising applications is graphically represented in Figure 1. In panel (a), we show that MSTLF consists of two elements: a Multi-Scale Texture Extractor (MSTE) (detailed in panel (b)) that extracts a textural representation obtained from the calculation of GLCMs at different spatial and angular scales, and an aggregation module (AM) that combines the textural representation into a scalar loss function \mathcal{L}_{txt} (panel (c)).

In the following, we provide a rigorous mathematical description of MSTLF in section 2.1, while we motivate the use of texture features in section 2.2. In section 2.3, we solve the problem of the non-differentiability of the GLCM by introducing a novel implementation based on soft assignments, that is compatible with gradient-based optimization frameworks.

2.1. Multi-Scale Texture Loss Function

Let's assume that $\mathbf{I} \in \mathbb{R}^{h \times w}$ and $\tilde{\mathbf{I}} \in \mathbb{R}^{h \times w}$ are a real and an approximated image, i.e., an image that belongs to the domain of interest and an image generated by a GAN, respectively, where h and w represent their height and width. Following Figure 1 (a), both \mathbf{I} and $\tilde{\mathbf{I}}$ are passed to the MSTE module to extract a multiscale textural representation based on GLCMs, i.e., \mathcal{H} and $\tilde{\mathcal{H}}$.

We now describe how to extract \mathcal{H} and $\tilde{\mathcal{H}}$. For fixed spatial and angular offset denoted as d and θ , respectively, the GLCM is defined as a squared matrix $\mathcal{G}_{d,\theta} \in \mathbb{R}^{n \times n}$, so that each element at coordinate (i, j) lies in the range $[0, 1]$. Each of its elements is computed as:

$$\mathcal{G}_{d,\theta}(i, j) = \frac{g_{d,\theta}(i, j)}{\sum_{i=1}^n \sum_{j=1}^n g_{d,\theta}(i, j)} \quad (2)$$

where,

$$g_{d,\theta}(i, j) = \sum_{x=1}^w \sum_{y=1}^h \delta[\mathbf{I}(x, y) = i] \cdot \delta[\mathbf{I}(\tilde{x}, \tilde{y}) = j] \quad (3)$$

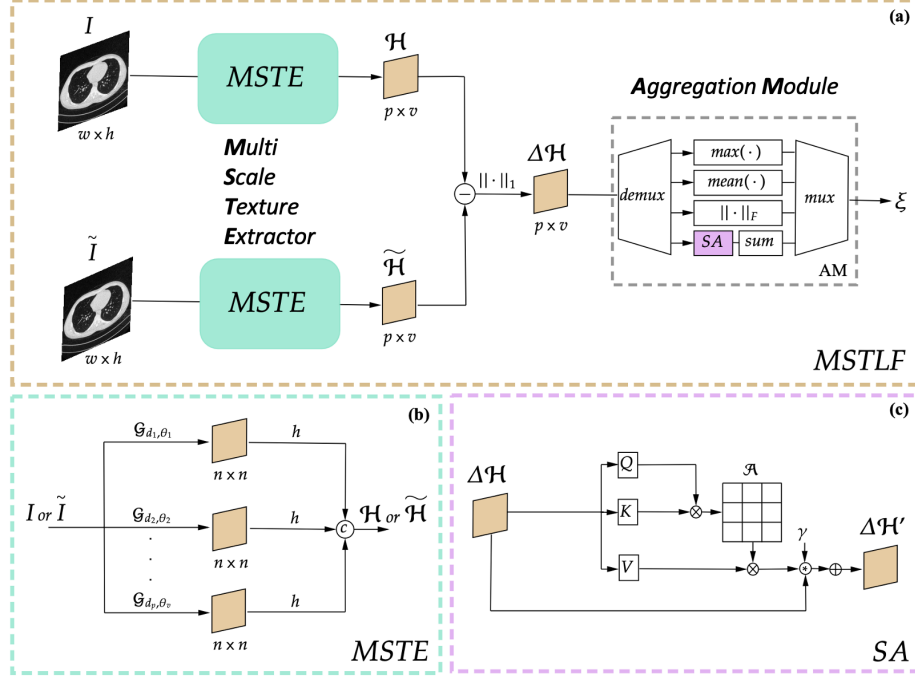


Figure 1: Overall framework of MSTLF. (a) MSTLF mainly includes two essential components, i.e., Multi-Scale Texture Extractor (MSTE) and Aggregation Module (AM). We denote the selection of the aggregation rule with the logic operators *demux* and *mux*. (b) MSTE module and (c) dynamic aggregation by Self-Attention mechanism (SA). First, MSTE extracts a textural representation from the GLCMs at different spatial and angular scales; second, AM combines the extracted representation into a scalar loss function.

s.t.

$$\tilde{x} = x + d \cos \theta \quad (4)$$

$$\tilde{y} = y + d \sin \theta \quad (5)$$

where δ is the Kronecker delta function, and $g_{d,\theta}(i, j)$ counts the occurrences of pixel value i and j .

Let $D = \{d_1, d_2, \dots, d_p\}$ and $\Theta = \{\theta_1, \theta_2, \dots, \theta_v\}$ be the sets of spatial and angular offsets, respectively. To obtain a multiscale texture representation (Figure 1 (b)) we consider the cartesian product between D and Θ :

$$D \times \Theta = \{(d_i, \theta_j) | d_i \in D, \theta_j \in \Theta\}, \quad (6)$$

Let's now assume that h is an operator extracting a texture descriptor from $\mathcal{G}_{d,\theta}(i, j)$ (more details in section 2.2).

We compute a multi-scale texture representation $\mathcal{H} \in \mathbb{R}^{p \times v}$ of \mathbf{I} as:

$$\mathcal{H} = \begin{bmatrix} h(\mathcal{G}_{d_1, \theta_1}) & \dots & \dots & \dots & \dots \\ \dots & \dots & \dots & \dots & \dots \\ \dots & \dots & h(\mathcal{G}_{d_i, \theta_j}) & \dots & \dots \\ \dots & \dots & \dots & \dots & \dots \\ \dots & \dots & \dots & \dots & h(\mathcal{G}_{d_p, \theta_v}) \end{bmatrix} \quad (7)$$

Similarly, for \mathbf{I} we compute $\tilde{\mathcal{H}} \in \mathbb{R}^{p \times v}$ (it is enough to replace \mathbf{I} with $\tilde{\mathbf{I}}$ in Eq. 3).

Going back to Figure 1 (a), we then compute the error deviation $\Delta\mathcal{H} \in \mathbb{R}^{p \times v}$ as:

$$\Delta\mathcal{H} = \|\mathcal{H} - \tilde{\mathcal{H}}\|_1. \quad (8)$$

The aggregation module AM combines textural information into a scalar ξ :

$$\xi = AM(\Delta\mathcal{H}). \quad (9)$$

We investigate two approaches for AM that we refer to as *static* and *dynamic* aggregation. In the first case, the aggregation is static because it is defined by mathematical operators performing the aggregation, as follows:

- Maximum: $\xi = \max(\Delta\mathcal{H})$, which leads the optimization to focus on the most discrepant texture descriptor.
- Average: $\xi = \text{mean}(\Delta\mathcal{H})$, which leads the optimization to focus on the average discrepancy among texture descriptors.
- Frobenius norm: $\xi = \|\Delta\mathcal{H}\|_F = \sqrt{\text{Tr}(\Delta\mathcal{H} \cdot \Delta\mathcal{H}^H)}$, similar to the average but performing a non-linear aggregation. Tr is the trace operator whilst H denotes the Hermitian operator.

In the second case, the aggregation is dynamic since it enables the model to adaptively capture relationships between texture descriptors during the training of the model. Inspired by Zhang et al. (2019), this approach is implemented as a self-attention layer (Fig. 1 (c)): $\Delta\mathcal{H}$ is passed through an attention layer which first applies 1×1 convolutions to extract keys \mathcal{K} , queries \mathcal{Q} and values \mathcal{V} . Then, the aggregation is computed as:

$$\xi = \langle \mathbf{1}_{p \cdot v}, \text{vec}(\Delta\mathcal{H}') \rangle \quad (10)$$

where,

$$\Delta\mathcal{H}' = \gamma \mathcal{A} \mathcal{V} + \Delta\mathcal{H} \quad (11)$$

s.t.

$$\mathcal{A} = \text{SoftMax}(\mathcal{Q}^T \mathcal{K}). \quad (12)$$

$\Delta\mathcal{H}' \in \mathbb{R}^{p \times v}$ is the output of the attention layer, $\mathbf{1}_{p \cdot v}$ is a vector of ones of size $p \cdot v$, $\text{vec}(\Delta\mathcal{H}')$ is the vectorized error deviation, $\langle \cdot, \cdot \rangle$ indicates the inner

product, $\mathcal{A} \in \mathbb{R}^{(p \cdot v) \times (p \cdot v)}$ denotes the attention map and γ is a trainable scalar weight.

Without loss of generality, we extend the derivation of our method to the entire image batch of size b :

$$\Xi = [\xi_1, \xi_2, \dots, \xi_b]^T \quad (13)$$

Then, the overall MSTLF is computed as:

$$\mathcal{L}_{txt} = \text{mean}(\Xi) = \frac{1}{b} \langle \mathbf{1}_b, \Xi \rangle \quad (14)$$

where $\mathbf{1}_b$ is a vector of ones of size b .

2.2. Which texture descriptor?

The texture descriptor h , introduced in section 2.1, can be expressed in different forms and, here, we rely on well-established Haralick features (Depeursinge et al. (2017)), namely the contrast, homogeneity, correlation, and angular second momentum, which are presented in Table 1. Denoting as $f(i, j)$ the term that gives a specific Haralick feature, we have for h

$$h(\mathcal{G}_{d,\theta}) = \sum_{i=1}^n \sum_{j=1}^n f(i, j) \mathcal{G}_{d,\theta}(i, j) \quad (15)$$

The same Table 1 reports the order of magnitude of Δh , i.e., the difference between LDCT and HDCT images captured by the Haralick feature h computed from 10 patients (not included in the other stages of this work) belonging to Mayo Clinic LDCT-and-Projection Data (Moen et al. (2021)), showing that contrast is the most sensitive to noise since it captures relative differences two orders of magnitude larger than the others. This could be expected as the contrast strictly depends on the noise in an image: indeed, the Contrast-to-Noise Ratio (CNR) of two regions A and B is equal to the absolute difference between their Signal-to-Noise Ratio SNR:

$$CNR_{AB} = \frac{|S_A - S_B|}{\sigma_N} = |SNR_A - SNR_B| \quad (16)$$

where S_A and S_B are the signals from image region A and B , and σ_N is the standard deviation of the noise. Hence, if we assume that the noise corruption over the entire image is approximately uniform, an increase in noise corresponds to a decrease in contrast.

2.3. How to make the GLCM differentiable

Differentiability is a key feature of any deep-learning framework. Whenever a new loss function or a regularization term is introduced, its implementation must be differentiable, i.e., it must be compatible with gradient-based optimization, enabling the backpropagation of the gradient throughout the entire model.

h	$f(i, j)$	Magnitude of Δh
Contrast	$(i - j)^2$	$\sim 10^2$
Homogeneity	$\frac{1}{1 - (i - j)^2}$	$\sim 10^{-2}$
Correlation	$\frac{(i - \mu_i)(j - \mu_j)}{\sqrt{\sigma_i^2 \sigma_j^2}}$	$\sim 10^{-3}$
Angular second moment	$\mathcal{G}_{d,\theta}(i, j)$	$\sim 10^{-2}$

Table 1: Definition of 4 well-established Haralick features and order of magnitude of the difference captured (Δh) between LDCT images and HDCT images computed from 10 patients (not included in the other stages of this work) belonging to Mayo Clinic LDCT-and-Projection Data (Moen et al. (2021)). The larger the value of Δh the higher the sensitivity to noise.

However, the GLCM is not differentiable by its very nature, since it is essentially a histogramming operation and hence it does not align with gradient-based optimization frameworks. For this reason, we propose a soft approximation of the GLCM which makes it a continuous and differentiable function.

To implement a differentiable GLCM, we employ a Gaussian soft assignment function for each pixel value to a set of predefined bins:

$$a_k(\mathbf{I}(x, y)) = e^{-\frac{(\mathbf{I}(x, y) - b_k)^2}{2\sigma^2}} \quad (17)$$

where $\mathbf{I}(x, y)$ is the pixel value in position (x, y) , b_k is the k^{th} bin value and σ is a hyperparameter denoting the standard deviation of the Gaussian assignment function. The latter is chosen due to its smooth bell-shaped curve, which helps in assigning weights to neighboring bins, ensuring a soft transition between them. Furthermore, σ controls the spread of the Gaussian: a lower σ creates sharper assignments (closer to hard binning), while a higher σ makes it softer, spreading the value across multiple bins. In our experiments, σ is set to 0.5 which results in a negligible error in the calculation of the soft GLCM of the order of $\sim 10^{-11}$. To ensure that the weights sum up to one, preserving the nature of probability, we normalize the soft assignment for each pixel with respect to all bins:

$$a'(\mathbf{I}(x, y)) = \frac{a_k}{\sum_{k=1}^n a_k(\mathbf{I}(x, y))} \quad (18)$$

Given two images (original \mathbf{I} and the corresponding spatially shifted $\mathbf{I}_{d,\theta}$ by the specified distance d and angle θ) and their soft assignments $a'(\mathbf{I}(x, y))$, the soft GLCM is obtained using the outer product:

$$\mathcal{G}_{d,\theta}^{i,j} = \sum_{x=1}^h \sum_{y=1}^w a'(\mathbf{I}(x, y)) \times a'(\mathbf{I}_s(x, y)) \quad (19)$$

where the outer product \times ensures that all possible combinations of pixel intensity relationships are considered, providing a comprehensive texture descriptor. It is worth noting that the entire process consists of differentiable operations, from Gaussian soft assignment to normalization and the outer product followed by summation, making the soft GLCM a differentiable function with respect to the input image \mathbf{I} . Furthermore, this method generalizes to any number of gray levels and can handle images of any bit depth without binning or down-scaling.

2.3.1. Computational Cost Analysis

Given that the Soft GLCM is a differentiable alternative to the traditional GLCM, it is crucial to analyze and compare the computational costs of these two methods.

The computational process of the traditional GLCM involves iterating through each pixel in the image and updating a co-occurrence count in the GLCM matrix. If the total number of pixels in the image is denoted as $N = h \cdot w$ and the size of the GLCM matrix as $n \times n$, the computation for each pixel pair is a constant time operation, $\mathcal{O}(1)$. Thus, the overall computational complexity of the traditional GLCM method scales linearly with the number of pixels, resulting in a complexity of $\mathcal{O}(N)$.

In contrast, the Soft GLCM incorporates a Gaussian soft assignment for each pixel value against a set of predefined bins, followed by the construction of the GLCM using these soft assignments. This procedure involves a two-fold computational process for each pixel: the soft assignment and the GLCM construction. In the soft assignment, each pixel value is subjected to a Gaussian computation against each bin, followed by a normalization step, incurring a complexity of $\mathcal{O}(n)$ per pixel. The construction of the GLCM from these soft assignments involves calculating the outer product of the soft assignment vectors of each pixel pair, resulting in a computational complexity of $\mathcal{O}(n^2)$ for each pixel. Aggregating these computations, the Soft GLCM presents a total computational complexity of $\mathcal{O}(N \cdot n^2)$, which is quadratic in the number of gray levels and linear in the number of pixels. We note that for images with high resolution or high bit depth, the Soft GLCM becomes significantly more computationally expensive compared to the traditional GLCM, but comes with the benefit of differentiability, which is crucial for gradient-based optimization in deep learning frameworks. This allows its integration into the deep learning framework, which enables leveraging parallel GPU tensor computations and batch-level processing, thus mitigating the computational overhead to a large extent.

3. Experimental Configuration

This section describes the deep models considered, the data used, the implementation details, and the evaluation metrics. Let us remember that $\mathbf{x} \in X$ is a LDCT image, whilst $\mathbf{y} \in Y$ is an HDCT image. To show the effectiveness of our method we validate our approach on three of the most widely used generative architectures (Pang et al. (2021)) in the image translation landscape: Pix2Pix (Isola et al. (2017)), CycleGAN (Zhu et al. (2017)), and UNIT (Liu et al. (2017)). The interested reader may refer to section 1 in the supplementary material for a detailed description of the three architectures.

3.1. Loss functions

We design experiments such that variations in performance are only attributed to variations in the loss function used. As shown in Table 2, we considered nine different configurations, where each configuration distinguishes from

	Experiment	Loss function
Competitors	Baseline	\mathcal{L}
	VGG-16	$\mathcal{L} + \mathcal{L}_{VGG}$
	AE-CT	$\mathcal{L} + \mathcal{L}_{AE}$
	SSIM-L	$\mathcal{L} + \mathcal{L}_{ssim}$
	EDGE	$\mathcal{L} + \mathcal{L}_{\nabla^2}$
Our approach	MSTLF-max	$\mathcal{L} + \mathcal{L}_{txt}^{max}$
	MSTLF-average	$\mathcal{L} + \mathcal{L}_{txt}^{avg}$
	MSTLF-Frobenius	$\mathcal{L} + \mathcal{L}_{txt}^{Frob}$
	MSTLF-attention	$\mathcal{L} + \mathcal{L}_{txt}^{att}$

Table 2: List of the proposed loss function configurations. For Pix2Pix, CycleGAN, and UNIT, the baseline loss function \mathcal{L} is implemented as reported in section 1 in the supplementary material.

the others by adding a loss function term to the baseline loss function \mathcal{L} . The first five configurations are competitors introduced in section 1, whilst the remaining four are different implementations of MSTLF that vary in the type of aggregation used to combine the texture descriptors.

For each model architecture, the first configuration is the baseline implemented in its original version reported in the supplementary material. The second is the perceptual loss function \mathcal{L}_{VGG-16} that is computed starting from the deep features extracted from the VGG-16 network (Simonyan and Zisserman (2014)), pre-trained on ImageNet (Russakovsky et al. (2015)). This loss term, originally introduced in (Gatys et al. (2015)), stems from observing that the similarity of features obtained from CNNs may indicate the level of semantic similarity between the images they come from providing an additional informative contribution compared to the traditional pixel-wise term (Pan et al. (2020)). Given a generic image \mathbf{I} and its approximation $\tilde{\mathbf{I}}$, \mathcal{L}_{VGG} is computed as (Johnson et al. (2016)):

$$\mathcal{L}_{VGG} = \frac{1}{W \cdot H \cdot D} \sum_{i=1}^5 \|\phi_i(\tilde{\mathbf{I}}) - \phi_i(\mathbf{I})\|_2^2 \quad (20)$$

where ϕ_i is the i^{th} pooling layer of the VGG-16 and W , H , D are its width, height, and depth, respectively.

As mentioned in section 1, deep feature extractors, pre-trained on ImageNet, can produce sub-optimal features when used in domains other than the natural image domain (Matsoukas et al. (2022)). For this reason, we implement a deep feature extractor trained on CT images (Han et al. (2021); Li et al. (2020a); Han et al. (2022)). We adopt the self-supervised approach proposed by (Li et al. (2020a)) that trains an auto-encoder network to extract an encoding from the input CT image that is then used to reconstruct an output CT image as close as possible to the input. We trained the auto-encoder with 8 patients (not included in the other stages of this work) for a total of 2824 images; among them, 4 belong to the Mayo Clinic LDCT-and-Projection Data (Moen et al.

(2021)) and the remaining 4 belong to the Lung Image Database Consortium and Image Database Resource Initiative (LIDC-IDRI) (Armato III (2011)). By utilizing data from two distinct datasets, we aimed to enhance the heterogeneity of the learned data distribution. We then use the encoded representation to compute the perceptual loss \mathcal{L}_{AE} (third row in Table 2):

$$\mathcal{L}_{AE} = \frac{\|e(\tilde{\mathbf{I}}) - e(\mathbf{I})\|_2^2}{W \cdot H \cdot D} \quad (21)$$

where e is the encoded representation and W , H , D are its width, height, and depth, respectively.

The fourth loss function is based on structural similarity (Wang et al. (2004)). \mathcal{L}_{ssim} , proposed as a more sophisticated and robust distance than the traditional L_1 and L_2 distances (Li et al. (2021, 2023); You et al. (2018)), is computed as:

$$\mathcal{L}_{ssim} = 1 - SSIM(\tilde{\mathbf{I}}, \mathbf{I}) \quad (22)$$

where $SSIM$ is the structural similarity index, described in section 3.3.

To overcome the limitations posed by L_1 and L_2 distances, some authors propose the use of the Charbonnier distance which is a smooth approximation of the Huber loss (Charbonnier et al. (1994); Gajera et al. (2021); Li et al. (2022); Kang et al. (2023)) that is quadratic for small variations and approximates the L_1 distance for large variations.

As fifth competitor, named edge loss, we use the Charbonnier distance \mathcal{L}_{∇^2} (Kyung et al. (2022); Zamir et al. (2021)), which minimizes the distance between Laplacians instead of pixel-intensities. It is given by:

$$\mathcal{L}_{\nabla^2} = \sqrt{\|\nabla^2(\tilde{\mathbf{I}}) - \nabla^2(\mathbf{I})\|^2 + \epsilon^2} \quad (23)$$

where ∇^2 denotes the Laplacian operator and ϵ^2 is a constant empirically set to 10^{-3} . It is also interesting to note that \mathcal{L}_{∇^2} catches a gradient-based quantity that maps edge information in the image, i.e., a feature different from the textural data we represent in our approach.

The last four loss functions shown in Table 2 are \mathcal{L}_{txt}^{max} , \mathcal{L}_{txt}^{avg} , \mathcal{L}_{txt}^{Frob} , \mathcal{L}_{txt}^{att} which differ in the type of aggregation used to combine texture descriptors. As mentioned in section 2.1, we have four approaches in the AM: three are static (maximum, average and Frobenius) and they are denoted as \mathcal{L}_{txt}^{max} , \mathcal{L}_{txt}^{avg} , \mathcal{L}_{txt}^{Frob} , respectively. The fourth, named \mathcal{L}_{txt}^{att} , is dynamic and it makes use of an attention mechanism. Before concluding this subsection, we detail how we apply MSTLF for each of the three GANs, graphically presented in Figure 2.

Without loss of generality, let \mathcal{L}_{txt} be a generic MSTLF. In Pix2Pix, we apply MSTLF between a generated image $\hat{\mathbf{y}} = G(\mathbf{x}, \mathbf{z})$ and its reference ground truth \mathbf{y} , i.e., $\mathcal{L}_{txt}(\hat{\mathbf{y}}, \mathbf{y})$ (Figure 2 (a)). In CycleGAN, we apply MSTLF to enforce the cycle consistency constraint between an image and its reconstruction in both the domains, i.e., $\mathcal{L}_{txt}(\hat{\mathbf{x}}, \mathbf{x})$, $\mathcal{L}_{txt}(\hat{\mathbf{y}}, \mathbf{y})$ where $\hat{\mathbf{x}} = F(G(\mathbf{x}))$ and $\hat{\mathbf{y}} = G(F(\mathbf{y}))$ are reconstructed images in the source domain X and the target domain Y , respectively (Figure 2 (b)). In UNIT, MSTLF is applied as, $\mathcal{L}_{txt}(\hat{\mathbf{x}}, \mathbf{x})$, $\mathcal{L}_{txt}(\hat{\mathbf{y}}, \mathbf{y})$ where $\hat{\mathbf{x}} = G_X(\hat{\mathbf{z}}_X)$ and $\hat{\mathbf{y}} = G_Y(\hat{\mathbf{z}}_Y)$ (Figure 2 (c)).

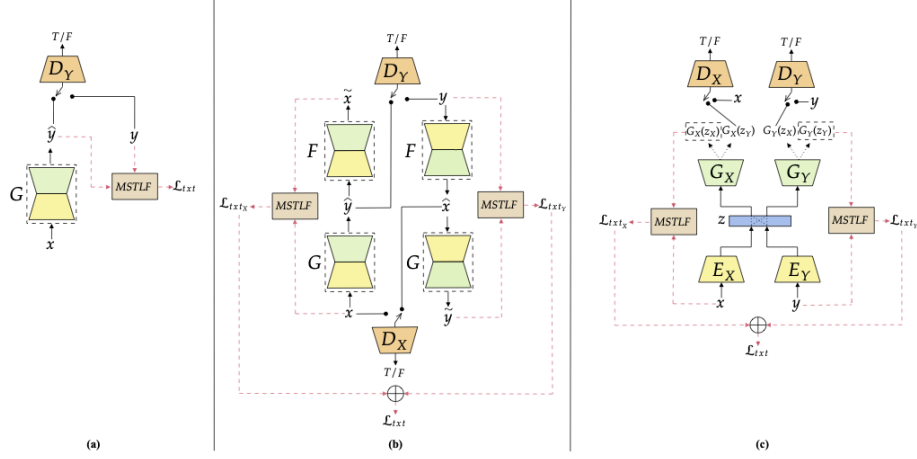


Figure 2: GAN architectures showing how MSTLF is applied. (a) Pix2Pix (b) CycleGAN (c) UNIT. The red dashed arrows denote the loss function computation. In UNIT, we use black dotted arrows to distinguish between different generation paths. G and F denotes generator networks, D_X and D_Y indicates discriminator networks, whilst E_X and E_Y are encoders and G_X and G_Y are decoders.

3.2. Materials

We use three public datasets that contain paired and unpaired images. The first is the Mayo Clinic LDCT-and-Projection Data (Moen et al. (2021)) which includes thoracic and abdominal HDCT and corresponding LDCT data simulated by a quarter dose protocol. We took 17 patients; among them, 10 are those used in the Mayo Clinic for the 2016 NIH-AAPM-Mayo Clinic Low Dose CT Grand Challenge¹ and 9 out of 10, corresponding to 5376 CT slices, are used for training as other works on LDCT denoising did (Li et al. (2020b); Tan et al. (2022); Ma et al. (2020); Li et al. (2021)). The test set, denoted as *Dataset A* in the following, contains 2994 slices from 8 patients: 1 patient from the aforementioned 10, plus other 7 patients randomly selected from (Moen et al. (2021)) to make the evaluation more robust.² The evaluation on the Mayo Clinic LDCT-and-Projection Data permits us to compute paired metrics reported in section 3.3, but it could be limited by the fact that LDCT images are simulated. To overcome this limitation we consider two real LDCT datasets that, straightforwardly, do not contain HDCT images. They are the Lung Image Database Consortium and Image Database Resource Initiative (LIDC/IDRI) (Armato III (2011)) and the ELCAP Public Image Database (Vision and I. A. Group (2009)), named *Dataset B* and *Dataset C* hereinafter. From the former, we included 8 patients for a total of 1831 LDCT images, whilst from the latter

¹<https://www.aapm.org/grandchallenge/lowdosect/>.

²The supplementary reports the list of patients' IDs used in this work from all three datasets.

we used the scans from 50 patients for a total of 12360 LDCT images.

3.3. Performance metrics

In (Di Feola et al. (2023)), they brought out that paired and unpaired metrics generally lead to different but complementary results, that is, they measure image quality from different perspectives. Here we used five image quality assessment metrics: Mean Square Error (MSE), Peak-Signal-to-Noise Ratio (PSNR), Structural Similarity Index (SSIM), Natural Image Quality Evaluator (NIQE), and Perception Based Image QUality Evaluator (PIQUE). The first three metrics perform a paired evaluation, i.e., they require pairs of images to be computed, whilst the last two relax this constraint performing a no-reference evaluation (Di Feola et al. (2023)). Both PSNR and MSE serve as error-based metrics, appropriate for quantifying the degree of image distortion without necessarily implying visually favorable outcomes. While SSIM has been introduced as a more sophisticated metric compared to the aforementioned two, it is better suited for measuring distortion rather than perception (Blau and Michaeli (2018); Tronchin et al. (2021)). Oppositely, NIQE and PIQUE are blind image quality assessment scores that only make use of measurable deviations measuring the perception (Mittal Anish (2012); Venkatanath et al. (2015)).

MSE

MSE computes the absolute difference between intensities in pixels of the denoised and reference image:

$$MSE(\hat{\mathbf{y}}, \mathbf{y}) = \frac{1}{mn} \sum_{i=0}^{m-1} \sum_{j=0}^{n-1} [\hat{\mathbf{y}}(i, j) - \mathbf{y}(i, j)]^2 \quad (24)$$

where (i, j) is the pixel coordinates, and m, n are the numbers of columns and rows, respectively. It ranges from 0 to $+\infty$. A lower MSE indicates a better match between the denoised and the reference image.

PSNR

PSNR compares the maximum intensity in the image ($MAX_{\hat{\mathbf{y}}}$) with the error between $\hat{\mathbf{y}}$ and \mathbf{y} given by the MSE:

$$PSNR(\hat{\mathbf{y}}, \mathbf{y}) = 10 \times \log_{10} \left(\frac{MAX_{\hat{\mathbf{y}}}^2}{MSE(\hat{\mathbf{y}}, \mathbf{y})} \right). \quad (25)$$

It ranges from 0 to $+\infty$ and it is expressed in decibels. Higher PSNR values indicate better quality, while lower values may suggest more noticeable distortions or errors in the denoised image.

SSIM

SSIM computes the local similarity between two images as a function of luminance, contrast, and structure (Wang et al. (2004)):

$$SSIM(\hat{\mathbf{y}}, \mathbf{y}) = \frac{(2\mu_{\hat{\mathbf{y}}}\mu_{\mathbf{y}} + C_1)(2\sigma_{\hat{\mathbf{y}}\mathbf{y}} + C_2)}{(\mu_{\hat{\mathbf{y}}}^2 + \mu_{\mathbf{y}}^2 + C_1)(\sigma_{\hat{\mathbf{y}}}^2 + \sigma_{\mathbf{y}}^2 + C_2)} \quad (26)$$

where $\mu_{\hat{\mathbf{y}}}$, $\mu_{\mathbf{y}}$ are mean intensities of pixels in $\hat{\mathbf{y}}$ and \mathbf{y} , respectively; similarly $\sigma_{\hat{\mathbf{y}}}^2$ and $\sigma_{\mathbf{y}}^2$ are the variances, $\sigma_{\hat{\mathbf{y}}\mathbf{y}}$ is the covariance whilst C_1 and C_2 are constant values to avoid numerical instabilities. It lies in $[0, 1]$ with values closer to 1 indicating better image quality.

NIQE

NIQE uses measurable deviations from statistical regularities observed in a corpus of natural images to quantify image perception, fitting a multivariate Gaussian model (Mittal Anish (2012)):

$$NIQE(\nu_1, \nu_{\hat{\mathbf{y}}}, \Sigma_1, \Sigma_{\hat{\mathbf{y}}}) = \left(\sqrt{(\nu_1 - \nu_{\hat{\mathbf{y}}})^T \left(\frac{\Sigma_1 + \Sigma_{\hat{\mathbf{y}}}}{2} \right)^{-1} (\nu_1 - \nu_{\hat{\mathbf{y}}})} \right) \cdot 100 \quad (27)$$

where ν_1 , Σ_1 , $\nu_{\hat{\mathbf{y}}}$, $\Sigma_{\hat{\mathbf{y}}}$ are the mean vectors and covariance matrices of the natural multivariate Gaussian model and the denoised image's multivariate Gaussian model, respectively. It lies in $[0, 100]$, with values closer to 0 indicating better image quality.

PIQUE

PIQUE measures perception in a denoised image exploiting local characteristics extracted from 16×16 non-overlapping blocks (Venkatanath et al. (2015)):

$$PIQUE(\hat{\mathbf{y}}) = \left(\frac{\left(\sum_{k=1}^{N_{SA}} D_{sk} \right) + C_1}{N_{SA} + C_1} \right) \cdot 100 \quad (28)$$

where D_{sk} captures the distortion of each image block, N_{SA} is the number of distorted blocks and C_1 is a constant to prevent numerical instability. It lies in $[0, 100]$, with values closer to 0 indicating better image quality.

3.4. Implementation Details

We preprocess all the images as follows: first, we convert all the raw DICOM files to Hounsfield Unit (HU), second, we select a display window centered in -500 HU with a width of 1400 HU, emphasizing lung tissue, third, we normalize all the images in the range $[-1, 1]$ and resized to 256×256 . The training dataset is paired, as mentioned in section 3.2: hence, we trained the Pix2Pix in a paired manner, while we trained CycleGAN and UNIT in an unpaired manner

by scrambling all the training images to avoid paired correspondence between HDCT and LDCT images for each training batch. We trained all the models for 50 epochs, with a batch size of 16. All the networks are initialized with normal initialization and optimized by Adam optimizer (Kingma and Ba (2014)) with default learning rates of $2 \cdot 10^{-4}$ for Pix2Pix and CycleGAN and 10^{-4} for UNIT. We set the weights of the baseline loss functions according to the original implementations, as described in the supplementary material. The weights of perceptual losses, edge loss, and SSIM loss were set to $\lambda_{VGG} = 0.1$, $\lambda_{AE-CT} = 10^3$, $\lambda_{EDGE} = 10$, $\lambda_{SSIM} = 1$, respectively. The weights of MSTLFs were set to $\lambda_{txt}^{max} = \lambda_{txt}^{avg} = \lambda_{txt}^{Frob} = 10^{-3}$, $\lambda_{txt}^{att} = 1$. The latter refers to MSTLF-attention and it was set to 1, as the self-attention layer incorporates its normalization and does not require external scaling. Our MSTLF used a set of spatial offsets $D = \{1, 3, 5, 7\}$ and a set of angular offsets $\Theta = \{0^\circ, 45^\circ, 90^\circ, 135^\circ\}$. All the models are parallelized on 4 NVIDIA Tesla A100, allowing for faster training time. We repeat each experiment three times to make the results more robust, mitigating the intrinsic variability that characterizes GANs’ training. We assess the average statistical significance of each experiment through the Wilcoxon Signed rank Test with $p < 0.05$.

4. Results and Discussion

This section performs an in-depth analysis to assess the effects of our MSTLF on LDCT denoising, providing both quantitative evaluations and visual examples.

Table 3 and Table 4 present the results of different experiments on simulated LDCT data (*Dataset A*), and real LDCT data (*Dataset B* and *C*), respectively. The two tables share the same structure: as a reference, the first row shows the values of the metrics computed on the LDCT images, which are used hereinafter to evaluate the relative improvement in image quality. The following rows are grouped in sections given the GAN backbone. For each section, there are nine experiments corresponding to the loss functions presented in section 3.1 and summarized in Table 2. In each section, we employ bold text and two asterisks to emphasize the best results per metric that exhibit statistically significant differences from the others. Additionally, we use bold text and a single asterisk to highlight the best results in a section that does not show statistically significant differences among themselves, while still satisfying $p < 0.05$ compared to the other experiments.

Both Table 3 and 4 show that the proposed MSTLF approach performs better than the other loss functions on all the architectures in most of the cases: indeed, MSTLF has the largest number of bold values denoting the best results per metric and per architecture. For each GAN backbone, the Wilcoxon Signed rank Test shows that these best results are always statistically different (except for one case in Table 4) from the others. This finding is also confirmed when performing the same test on a per-patient basis, as shown in section 5 of the supplementary.

Experiment		Dataset A				
		PSNR \uparrow	MSE \uparrow	SSIM \uparrow	NIQE \downarrow	PIQUE \downarrow
LDCT	-	17.7322	$2.25 \cdot 10^{-3}$	0.5832	17.0272	23.5495
Pix2Pix	Baseline	21.3344	$10.50 \cdot 10^{-3}$	0.7335	6.5263	8.6017
	VGG-16	21.3481	$10.41 \cdot 10^{-3}$	0.7293	6.5673	8.7114
	AE-CT	21.3422	$10.55 \cdot 10^{-3}$	0.7349	6.1640	8.9156
	SSIM-L	21.4011	$10.37 \cdot 10^{-3}$	0.7426**	6.0690	8.2995
	EDGE	21.0620	$10.63 \cdot 10^{-3}$	0.7196	6.4413	8.7461
	MSTLF-max	21.3234	$10.50 \cdot 10^{-3}$	0.7284	6.5024	8.7950
	MSTLF-average	21.4497**	$10.32 \cdot 10^{-3**}$	0.7379	6.2366	8.5473
	MSTLF-Frobenius	21.3661	$10.42 \cdot 10^{-3}$	0.7347	6.0670	8.8096
	MSTLF-attention	20.7495	$11.62 \cdot 10^{-3}$	0.7103	5.1934**	7.3575**
CycleGAN	Baseline	20.8588	$10.15 \cdot 10^{-3}$	0.6935	9.6203	12.6893
	VGG-16	20.7759	$10.17 \cdot 10^{-3}$	0.6997	10.1728	13.3256
	AE-CT	21.2143	$9.69 \cdot 10^{-3}$	0.7092	8.0317	8.7166
	SSIM-L	20.6699	$10.50 \cdot 10^{-3}$	0.6919	10.2733	13.0187
	EDGE	20.5538	$10.84 \cdot 10^{-3}$	0.6928	10.7092	13.5882
	MSTLF-max	20.9735	$9.70 \cdot 10^{-3}$	0.7013	9.2843	11.9323
	MSTLF-average	21.2529**	$9.32 \cdot 10^{-3**}$	0.7114**	8.6642	10.9737
	MSTLF-Frobenius	21.1883	$9.54 \cdot 10^{-3}$	0.7108	8.5100	11.1255
	MSTLF-attention	20.6741	$9.89 \cdot 10^{-3}$	0.7058	5.3209**	5.4432**
UNIT	Baseline	21.4333	$8.85 \cdot 10^{-3}$	0.7203	6.4581	8.3179
	VGG-16	21.4207	$8.54 \cdot 10^{-3}$	0.7296	6.5030	7.7908
	AE-CT	22.0836	$7.68 \cdot 10^{-3}$	0.7450	7.2524	7.6388
	SSIM-L	22.1704	$7.64 \cdot 10^{-3}$	0.7465	7.4184	7.5623
	EDGE	21.9671	$7.83 \cdot 10^{-3}$	0.7434	6.6897	7.2272**
	MSTLF-max	22.2671**	$7.32 \cdot 10^{-3**}$	0.7480**	6.8441	7.5657
	MSTLF-average	22.0836	$7.70 \cdot 10^{-3}$	0.7429	6.7520	7.8877
	MSTLF-Frobenius	22.1601	$7.41 \cdot 10^{-3}$	0.7458	7.1659	7.7813
	MSTLF-attention	22.1270	$7.39 \cdot 10^{-3}$	0.7426	6.0238**	7.4101

Table 3: Quantitative comparison of different loss function configurations on the simulated test set. The numerical values are the average values over three repetitions of each experiment. Bold text and two asterisks denote best results per metric and per architecture satisfying $p < 0.05$; bold text and a single asterisk highlight the best results in a section with $p \geq 0.05$ among themselves, while satisfying $p < 0.05$ wrt to the other experiments.

In Pix2Pix, MSTLF-average outperforms the other loss function configurations in terms of PSNR and MSE, while SSIM-L reaches the highest SSIM score, which is expected since SSIM-L is meant to maximize the SSIM. MSTLF-attention achieves the best result in NIQE and PIQUE on *Dataset A*, *B*, and *C*, proving to be effective on both simulated LDCT data and real LDCT data.

Turning our attention to the results attained using the CycleGAN, the results are consistent with those of Pix2Pix: MSTLF-average outperforms the other loss function configurations in all paired metrics while MSTLF-attention reaches the best performance in terms of unpaired metrics (NIQE and PIQUE) on all the datasets.

In UNIT, MSTLF-max is the best configuration focusing on paired metrics, while MSTLF-attention stands out in NIQE, as in Pix2Pix and CycleGAN. The best PIQUE instead is achieved by EDGE which, however, does not excel in any other metrics or architectures. On the contrary, MSTLF shows consistency of results on most metrics regardless of the architecture, showcasing a higher degree

Experiment		Dataset B		Dataset C	
		NIQE ↓	PIQUE ↓	NIQE ↓	PIQUE ↓
LDCT	-	13.6189	20.3687	11.8081	15.1818
Pix2Pix	Baseline	5.5597	8.9952	5.4423	6.9620
	VGG-16	5.5726	8.8453	5.4671	6.8522
	AE-CT	5.1338	8.4187	5.0586	6.4835
	SSIM-L	5.1439	8.3272	5.1091	6.2623*
	EDGE	5.5052	9.5456	5.6078	7.4611
	MSTLF-max	5.5234	9.0999	5.4585	7.061
	MSTLF-average	5.2658	8.7173	5.2390	6.6374
	MSTLF-Frobenius	5.1832	8.5485	5.1944	6.7230
	MSTLF-attention	4.8728**	7.3443**	4.8634**	6.2841*
CycleGAN	Baseline	8.6468	12.6395	8.3811	10.5286
	VGG-16	8.3012	10.9972	8.1010	9.0185
	AE-CT	7.1581	7.3931	6.9573	6.5963
	SSIM-L	8.9653	12.2665	8.7280	10.2850
	EDGE	8.9325	12.4375	8.6059	10.3436
	MSTLF-max	8.3655	11.7319	8.1205	9.9322
	MSTLF-average	7.9853	11.6693	7.8831	9.9328
	MSTLF-Frobenius	7.5627	10.8876	7.4276	9.0732
	MSTLF-attention	5.1713**	6.2002**	5.1967**	5.7071**
UNIT	Baseline	5.9253	9.0455	5.9474	7.4220
	VGG-16	5.9518	9.0618	5.9586	7.4170
	AE-CT	6.7394	8.8963	6.6581	7.1964
	SSIM-L	7.0960	8.5735	7.0274	6.9753
	EDGE	6.4342	7.9593**	6.3607	6.5470**
	MSTLF-max	6.5491	8.4952	6.5070	6.8747
	MSTLF-average	6.4214	9.1836	6.4317	7.4392
	MSTLF-Frobenius	6.6947	8.9574	6.6231	7.2449
	MSTLF-attention	5.5228**	8.5232	5.5433**	7.0860

Table 4: Quantitative comparison of different loss function configurations on the real test sets. The numerical values are the average values over three repetitions of each experiment. Bold text and two asterisks denote best results per metric and per architecture satisfying $p < 0.05$; bold text and a single asterisk highlight the best results in a section with $p \geq 0.05$ among themselves, while satisfying $p < 0.05$ wrt to the other experiments.

of agnosticism compared to other loss functions. We further observe that configurations that perform a static aggregation, i.e., MSTLF-max, MSTLF-average, MSTLF-Frobenius, favor paired metrics, whilst MSTLF-attention, performing dynamic aggregation, favors unpaired metrics.

Figure 3 shows an example of denoised images on *Dataset A* using the CycleGAN backbone. In panel (a) we report the HDCT and LDCT images followed by synthetic images provided by the nine experiments, whilst panel (b) shows the gradient of these images, to highlight noise in the image. For the sake of visualization, panel (c) shows the zoomed Regions Of Interest (ROIs) identified by the red boxes in the gradient images, which contain areas inside and out-

side the lung regions, thus including different tissues and anatomical structures. It is worth noting that MSTLF-attention produced the image with the lowest gradient that, in turn, corresponds to the lowest level of noise while preserving the lung boundaries (MSTLF-attention in Figure 3 (c)). Section 2 in the supplementary material completes the visual examples showing the results for the other two datasets and GAN backbones.

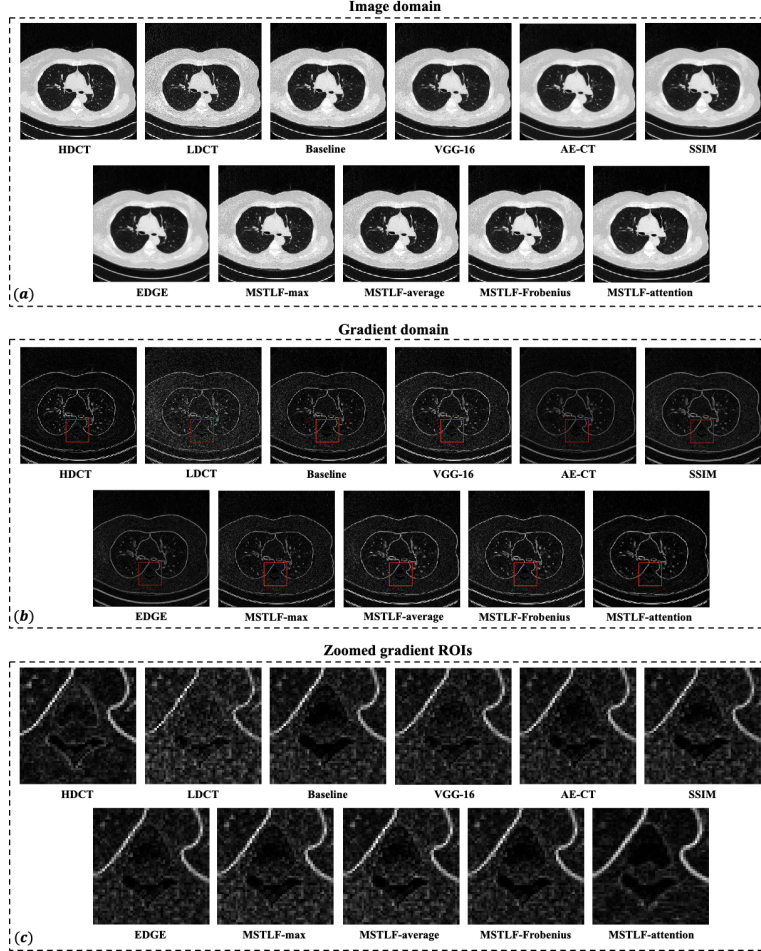


Figure 3: Visual comparison of denoised CT slices from the Mayo simulated data (*Dataset A*). We show all loss function configurations for CycleGAN (see supplementary for the remaining figures relative to CycleGAN, Pix2Pix and UNIT). The images are shown both in the image domain (panel (a)) using a display window in $[-1200, 200]$ HU), and the gradient domain (panel (b)). The zoomed ROI in panel (c) highlights denoising in the gradient domain.

4.1. The Perception-Distortion Trade-Off

Blau and Michaeli (2018) demonstrated that there exists a trade-off between

perception and distortion when dealing with image restoration algorithms, that is, a low average distortion not necessarily implies a good perceptual quality and achieving both is an open challenge. From this consideration, we now look at our results from a perception-distortion perspective; as reported in section 3.3, perception is measured by NIQE and PIQUE, whereas distortion is measured by the MSE. Accordingly we represent each experiment by a point in the two perception-distortion planes (panels (a) and (b) of Figure 4). Then, we assess the trade-off between perception and distortion by ranking the experiments based on their proximity to the origin, as the point (0,0) is the ideal one (Table 5). We find that MSTLF-attention is the one that reaches the best trade-off between perception and distortion, demonstrating consistent performance across different architectures. This outcome further supports the agnostic nature of our approach with respect to the GAN architecture.

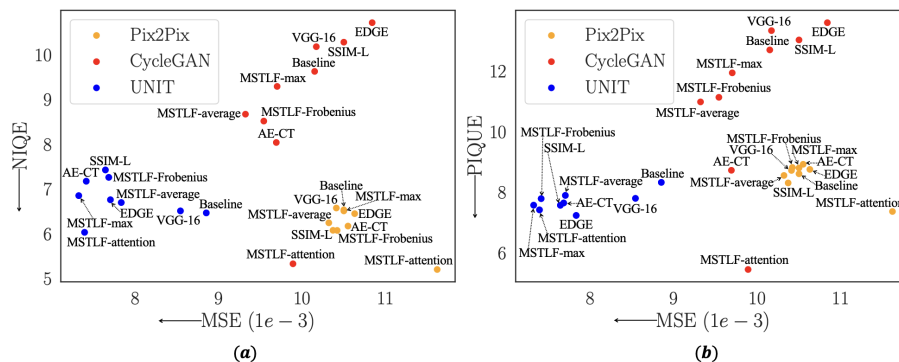


Figure 4: Perception-distortion evaluation of denoising algorithms. We plot the 9 experiments detailed in Table 3.1 on the perception distortion plane. The color legend groups the experiments based on the GAN architecture. Distortion is measured by MSE in both panels, whilst perception is measured by NIQE and PIQUE in panel (a) and panel (b), respectively.

Experiment	NIQE vs MSE ranking				PIQUE vs MSE ranking			
	Pix2Pix	CycleGAN	UNIT	Global	Pix2Pix	CycleGAN	UNIT	Global
Baseline	8	6	2	45	4	6	9	50
VGG-16	9	7	3	49	5	8	7	50
AE-CT	4	2	8	26	9	2	5	36
SSIM-L	3	8	9	31	2	7	3	36
EDGE	6	9	4	35	6	9	1	44
MSTLF-max	7	5	6	49	7	5	4	47
MSTLF-average	5	4	5	44	3	3	8	44
MSTLF-Frobenius	2	3	7	42	8	4	6	49
MSTLF-attention	1	1	1	6	1	1	1	8

Table 5: Distance ranking in the perception-distortion plane.

4.2. Template Matching Analysis

To gain more insight into the denoising performance, we perform an analysis that quantifies the LDCT noise pattern still present in the corresponding denoised version. To this aim, let us remember that \mathbf{x} is a LDCT image resized to 256×256 (see section 3.4), now belonging to a set of d test images. Furthermore, $\mathbf{T} \in \mathbf{x}$ denotes a template of size $t \times t$ (with $t = 32$) extracted from \mathbf{x} at a given location. To quantify the aforementioned noise pattern we proceed as follows. First, we compute the maximum template matching between \mathbf{T} and the denoised image $\hat{\mathbf{y}}$ given by

$$m = \max(\mathbf{M}(x, y)) \text{ with } x, y \in [0, 255] \quad (29)$$

where $\mathbf{M}(x, y)$ is the template matching at location (x, y) calculated using zero-padding as

$$\mathbf{M}(x, y) = \frac{\sum_{x', y'} \mathbf{T}(x', y') \cdot \hat{\mathbf{y}}(x + x', y + y')}{\sqrt{\sum_{x', y'} \mathbf{T}(x', y')^2 \cdot \sum_{x', y'} \hat{\mathbf{y}}(x + x', y + y')^2}} \quad (30)$$

noticing that $\hat{\mathbf{y}}$ stands for the denoised image, and x', y' represent the discrete unitary displacement, ranging in $[0, t - 1]$, with respect to the current position (x, y) . Hence, the numerator computes the cross-correlation between \mathbf{T} and $\hat{\mathbf{y}}$, whilst the denominator is a normalization term.

Second, in order not to limit the analysis to a single image region in the original LDCT, we extract $r = 9$ equispaced templates obtaining r matching scores m . Given d LDCT images, we collect $r \cdot d$ matching scores that we use to estimate the underlying matching distribution through kernel density estimation:

$$\hat{f}(m) = \frac{1}{(r \cdot d) \cdot h} \sum_{i=1}^{r \cdot d} K\left(\frac{m - m_i}{h}\right) \quad (31)$$

where $\hat{f}(m)$ is the estimated probability density function, K is a Gaussian kernel function and h is a non-negative smoothing parameter that can be estimated using Scott's rule (Scott (2015)).

Figure 5 presents the results and is organized as follows: each row corresponds to a dataset from A to C , and it contains three panels, one for each GAN. In each panel, the matching distribution computed over the LDCT images is a delta function (in red) since all the templates come from the same LDCT images and, so, the matching scores are all equal to 1. In the first row we use a paired dataset and we, therefore, report in light blue the matching distribution between the LDCT templates and the HDCT images, which provides us with a lower boundary reference to assess any other matching distribution computed between the LDCT templates and the denoised images. The visual inspection of the 9 plots confirms that MSTLF-attention is the best configuration. Indeed, looking at Figure 5 (a)-(b)-(c), MSTLF-attention turns out to be the distribution that tends more toward the high-dose reference. Even in Figure 5 (d)-(e)-(f)-(g)-(h)-(i), that do not report the high-dose reference,

we notice that MSTLF-attention deviates more than other approaches from the low-dose reference. The plots in Figure 5 (b)-(e)-(h) also reveal that AE-CT has the closest behavior to MSTLF-attention, thus supporting the effectiveness and superiority of domain-specific deep features over ImageNet features. Indeed, the widely adopted VGG-16 perceptual loss does not excel in any of our analyses. Nonetheless, AE-CT is second in position to MSTLF-attention only in CycleGAN and if we look at the previous analysis it excels only in terms of NIQE (Table 3 and 4) without reaching a satisfying perception-distortion trade-off (Figure 4 and Table 5). In Figure 5 (c) we observe that all configurations, including MSTLF-attention, remain distant from the high-dose boundary. We interpret this result as the tendency for UNIT to favor distortion rather than perception. Indeed, among the architectures, UNIT is the one that reaches the best PSNR, MSE, and SSIM (see Table 3).

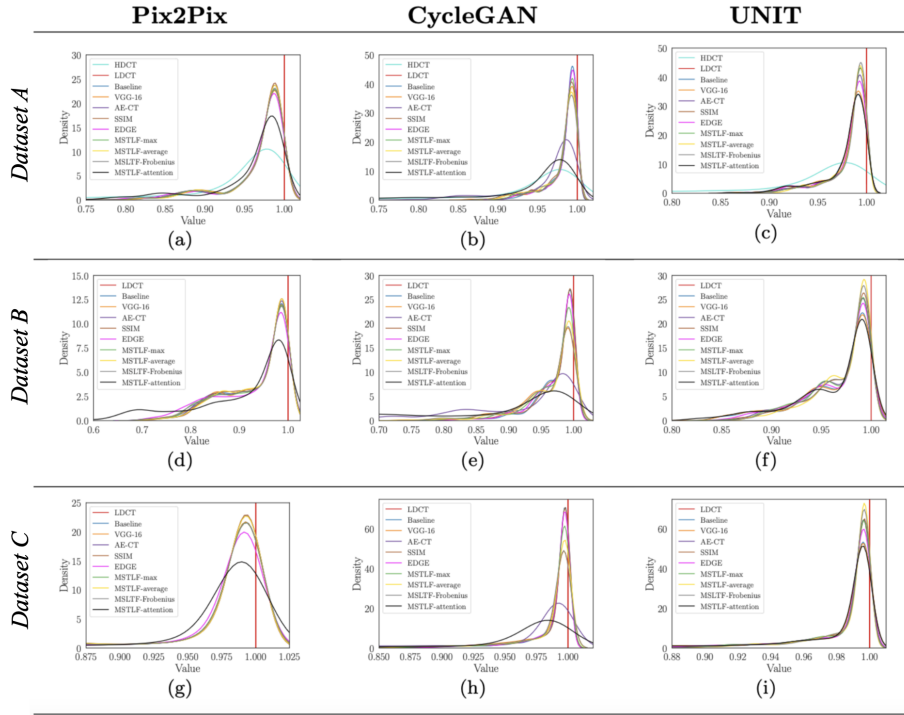


Figure 5: Template matching analysis. Each panel illustrates the matching distributions between the noisy templates extracted from the LDCT images and the denoised images.

4.3. Computational Analysis

Table 6 shows the computational analysis, where the computation time is given by the average time over one training epoch needed to compute the loss function and to back-propagate its gradient. In general, both CycleGAN and UNIT are more computationally demanding ($\sim 70\%$ more than Pix2Pix): this is expected since these two GANs have larger architectures than Pix2Pix, and also because they compute the loss term twice when performing the bidirectional translation between LD and HD domains. Both VGG-16 and AE-CT cause an increase in computational burden compared to the baseline (up to $+36\%$) since they use a VGG-16 network and an auto-encoder as feature extractors, respectively. Although these networks are frozen, the back-propagation is always computed, hence affecting the overall computation time. On the contrary, SSIM-L and EDGE have the same computation time as the baseline since they introduce two loss terms that rely on mathematical operations applied to the images without additional cost for back-propagating the gradient. Turning our attention to our MSTLFs, these cause a significant increase in computation time (up to $+65\%$ with respect to the baseline) due to the complexity of the operations that extract a multi-scale texture representation exploiting the soft GLCMs. Indeed, ensuring compatibility with the gradient-based optimization frameworks leads to an implementation that is more computationally onerous than the standard GLCM (section 2.3). Nonetheless, we notice that the type of aggregation used does not significantly affect the computational burden. In this regard, static aggregation, which is defined by mathematical operators, has the same impact as dynamic aggregation defined by self-attention. Such observation combined with the good performance reached by MSTLF-attention makes dynamic aggregation a promising approach.

Experiment	Pix2Pix	CycleGAN	UNIT
Baseline	0.09 s	0.42 s	0.28 s
VGG-16	0.13 s	0.49 s	0.44 s
AE-CT	0.11 s	0.47 s	0.41 s
SSIM	0.09 s	0.42 s	0.28 s
EDGE	0.09 s	0.42 s	0.28 s
MSTLF-max	0.26 s	0.89 s	0.81 s
MSTLF-average	0.26 s	0.94 s	0.82 s
MSTLF-Frobenius	0.26 s	0.95 s	0.82 s
MSTLF-attention	0.26 s	1.01 s	0.84 s

Table 6: Computational analysis. The computation time is expressed as the average time required to compute the loss function and to back-propagate its gradient for each batch.

5. Conclusions

In this paper, we present an approach, named MSTLF, for GAN-based denoising in CT imaging that embeds textural information, extracted at different

spatial and angular scales. We also overcome the limitations posed by the non-differentiability of the GLCM proposing a novel implementation based on soft assignment that makes it compatible with gradient-based optimization frameworks. Our comprehensive analysis on three datasets and three GANs backbones brings out the effectiveness of MSTLF to enhance the quality of LDCT images. In particular, the configuration exploiting the attention layer to dynamically aggregate multi-scale texture data attains the best performance compared to other well-established loss functions. We also find two other interesting results. First, it also successfully tackles the challenging trade-off between distortion and perception. Second, just as it tailors the aggregation to the specific needs of the optimization process, it also succeeds in adapting the GAN architecture used. Future works are directed towards further investigation of the backbone-independent feature of the MSTLF, testing its application in other denoising frameworks in medical and non-medical applications.

Acknowledgments

Resources are provided by the National Academic Infrastructure for Supercomputing in Sweden (NAISS) and the Swedish National Infrastructure for Computing (SNIC) at Alvis @ C3SE, partially funded by the Swedish Research Council through grant agreements no. 2022-06725 and no. 2018-05973. We acknowledge financial support from: i) PNRR MUR project PE0000013-FAIR, ii) PRIN 2022 MUR 20228MZFAA-AIDA (CUP C53D23003620008), iii) PRIN PNRR 2022 MUR P2022P3CXJ-PICTURE (CUP C53D23009280001).

References

- Aharon, M., Elad, M., Bruckstein, A., 2006. K-SVD: An algorithm for designing overcomplete dictionaries for sparse representation. *IEEE Transactions on signal processing* 54, 4311–4322.
- Armato III, Samuel G, M., 2011. The lung image database consortium (LIDC) and image database resource initiative (IDRI): a completed reference database of lung nodules on CT scans. *Medical physics* 38, 915–931.
- Bera, S., Biswas, P.K., 2023. Self Supervised Low Dose Computed Tomography Image Denoising Using Invertible Network Exploiting Inter Slice Congruence, in: *Proceedings of the IEEE/CVF Winter Conference on Applications of Computer Vision*, pp. 5614–5623.
- Bevelacqua, J.J., 2010. Practical and effective ALARA. *Health physics* 98, S39–S47.
- Blau, Y., Michaeli, T., 2018. The perception-distortion tradeoff, in: *Proceedings of the IEEE conference on computer vision and pattern recognition*, pp. 6228–6237.

- Brenner, D.J., Hall, E.J., 2007. Computed tomography—an increasing source of radiation exposure. *New England journal of medicine* 357, 2277–2284.
- Burgos, N., Svoboda, D., 2022. *Biomedical Image Synthesis and Simulation: Methods and Applications*. Academic Press.
- Charbonnier, P., Blanc-Feraud, L., Aubert, G., Barlaud, M., 1994. Two deterministic half-quadratic regularization algorithms for computed imaging, in: *Proceedings of 1st international conference on image processing, IEEE*. pp. 168–172.
- Dabov, K., Foi, A., Katkovnik, V., Egiazarian, K., 2007. Image denoising by sparse 3-D transform-domain collaborative filtering. *IEEE Transactions on image processing* 16, 2080–2095.
- Depeursinge, A., Omar, S., Al, K., Mitchell, J.R., 2017. *Biomedical texture analysis: fundamentals, tools and challenges*. Academic Press.
- Di Feola, F., Tronchin, L., Soda, P., 2023. A comparative study between paired and unpaired image quality assessment in low-dose ct denoising, in: *2023 IEEE 36th International Symposium on Computer-Based Medical Systems (CBMS)*, pp. 471–476. doi:[10.1109/CBMS58004.2023.00264](https://doi.org/10.1109/CBMS58004.2023.00264).
- Du, W., Chen, H., Liao, P., Yang, H., Wang, G., Zhang, Y., 2019. Visual attention network for low-dose CT. *IEEE Signal Processing Letters* 26, 1152–1156.
- Elad, M., Kwar, B., Vaksman, G., 2023. Image denoising: The deep learning revolution and beyond—a survey paper. *SIAM Journal on Imaging Sciences* 16, 1594–1654.
- Gajera, B., Kapil, S.R., Ziaei, D., Mangalagiri, J., Siegel, E., Chapman, D., 2021. CT-scan denoising using a charbonnier loss generative adversarial network. *IEEE Access* 9, 84093–84109.
- Gatys, L., Ecker, A.S., Bethge, M., 2015. Texture synthesis using convolutional neural networks. *Advances in neural information processing systems* 28.
- Han, M., Shim, H., Baek, J., 2021. Low-dose CT denoising via convolutional neural network with an observer loss function. *Medical physics* 48, 5727–5742.
- Han, M., Shim, H., Baek, J., 2022. Perceptual CT loss: implementing CT image specific perceptual loss for CNN-based low-dose CT denoiser. *IEEE Access* 10, 62412–62422.
- Huang, Z., Zhang, J., Zhang, Y., Shan, H., 2021. DU-GAN: Generative adversarial networks with dual-domain U-Net-based discriminators for low-dose CT denoising. *IEEE Transactions on Instrumentation and Measurement* 71, 1–12.

- Isola, P., Zhu, J.Y., Zhou, T., Efros, A.A., 2017. Image-to-image translation with conditional adversarial networks, in: Proceedings of the IEEE conference on computer vision and pattern recognition, pp. 1125–1134.
- Izadi, S., Sutton, D., Hamarneh, G., 2023. Image denoising in the deep learning era. *Artificial Intelligence Review* 56, 5929–5974.
- Johnson, J., Alahi, A., Fei-Fei, L., 2016. Perceptual losses for real-time style transfer and super-resolution, in: Computer Vision–ECCV 2016: 14th European Conference, Amsterdam, The Netherlands, October 11–14, 2016, Proceedings, Part II 14, Springer. pp. 694–711.
- Kang, J., Liu, Y., Shu, H., Guo, N., Zhang, Q., Zhou, Y., Gui, Z., 2023. Gradient extraction based multiscale dense cross network for LDCT denoising. *Nuclear Instruments and Methods in Physics Research Section A: Accelerators, Spectrometers, Detectors and Associated Equipment* 1055, 168519.
- Kaur, A., Dong, G., 2023. A complete review on image denoising techniques for medical images. *Neural Processing Letters* 55, 7807–7850.
- Kingma, D.P., Ba, J., 2014. Adam: A method for stochastic optimization. *arXiv preprint arXiv:1412.6980*.
- Kwon, T., Ye, J.C., 2021. Cycle-free cyclegan using invertible generator for unsupervised low-dose ct denoising. *IEEE Transactions on Computational Imaging* 7, 1354–1368.
- Kyung, S., Won, J., Pak, S., Hong, G.s., Kim, N., 2022. MTD-GAN: Multi-task Discriminator Based Generative Adversarial Networks for Low-Dose CT Denoising, in: International Workshop on Machine Learning for Medical Image Reconstruction, Springer. pp. 133–144.
- Li, M., Hsu, W., Xie, X., Cong, J., Gao, W., 2020a. SACNN: Self-attention convolutional neural network for low-dose CT denoising with self-supervised perceptual loss network. *IEEE transactions on medical imaging* 39, 2289–2301.
- Li, S., Li, Q., Li, R., Wu, W., Zhao, J., Qiang, Y., Tian, Y., 2022. An adaptive self-guided wavelet convolutional neural network with compound loss for low-dose CT denoising. *Biomedical Signal Processing and Control* 75, 103543.
- Li, Z., Liu, Y., Shu, H., Lu, J., Kang, J., Chen, Y., Gui, Z., 2023. Multi-Scale Feature Fusion Network for Low-Dose CT Denoising. *Journal of Digital Imaging*, 1–18.
- Li, Z., Shi, W., Xing, Q., Miao, Y., He, W., Yang, H., Jiang, Z., 2021. Low-dose CT image denoising with improving WGAN and hybrid loss function. *Computational and Mathematical Methods in Medicine* 2021.

- Li, Z., Zhou, S., Huang, J., Yu, L., Jin, M., 2020b. Investigation of low-dose CT image denoising using unpaired deep learning methods. *IEEE transactions on radiation and plasma medical sciences* 5, 224–234.
- Liu, M.Y., Breuel, T., Kautz, J., 2017. Unsupervised image-to-image translation networks. *Advances in neural information processing systems* 30.
- Ma, Y., Wei, B., Feng, P., He, P., Guo, X., Wang, G., 2020. Low-dose CT image denoising using a generative adversarial network with a hybrid loss function for noise learning. *IEEE Access* 8, 67519–67529.
- Marcos, L., Alirezaie, J., Babyn, P., 2021. Low dose CT image denoising using boosting attention fusion gan with perceptual loss, in: 2021 43rd Annual International Conference of the IEEE Engineering in Medicine & Biology Society (EMBC), IEEE. pp. 3407–3410.
- Matsoukas, C., Haslum, J.F., Sorkhei, M., Söderberg, M., Smith, K., 2022. What makes transfer learning work for medical images: Feature reuse & other factors, in: *Proceedings of the IEEE/CVF Conference on Computer Vision and Pattern Recognition*, pp. 9225–9234.
- Mittal Anish, Rajiv Soundararajan, A.C.B., 2012. Making a “completely blind” image quality analyzer. *IEEE Signal processing letters* 20, 209–212.
- Moen, T.R., Chen, B., Holmes III, D.R., Duan, X., Yu, Z., Yu, L., Leng, S., Fletcher, J.G., McCollough, C.H., 2021. Low-dose CT image and projection dataset. *Medical physics* 48, 902–911.
- Ohno, Y., Koyama, H., Seki, S., Kishida, Y., Yoshikawa, T., 2019. Radiation dose reduction techniques for chest CT: principles and clinical results. *European journal of radiology* 111, 93–103.
- Pan, Z., Yu, W., Wang, B., Xie, H., Sheng, V.S., Lei, J., Kwong, S., 2020. Loss functions of generative adversarial networks (GANs): Opportunities and challenges. *IEEE Transactions on Emerging Topics in Computational Intelligence* 4, 500–522.
- Pang, Y., Lin, J., Qin, T., Chen, Z., 2021. Image-to-image translation: Methods and applications. *IEEE Transactions on Multimedia* 24, 3859–3881.
- Park, H.S., Baek, J., You, S.K., Choi, J.K., Seo, J.K., 2019. Unpaired image denoising using a generative adversarial network in X-ray CT. *IEEE Access* 7, 110414–110425.
- Park, H.S., Jeon, K., Lee, J., You, S.K., 2022. Denoising of pediatric low dose abdominal CT using deep learning based algorithm. *Plos one* 17, e0260369.
- Russakovsky, O., Deng, J., Su, H., Krause, J., Satheesh, S., Ma, S., Huang, Z., Karpathy, A., Khosla, A., Bernstein, M., Berg, F.F., 2015. Imagenet large scale visual recognition challenge. *International journal of computer vision* 115, 211–252.

- Santucci, D., Faiella, E., Cordelli, E., Sicilia, R., de Felice, C., Zobel, B.B., Iannello, G., Soda, P., 2021. 3T MRI-radiomic approach to predict for lymph node status in breast cancer patients. *Cancers* 13, 2228.
- Scott, D.W., 2015. Multivariate density estimation: theory, practice, and visualization. John Wiley & Sons.
- Simonyan, K., Zisserman, A., 2014. Very deep convolutional networks for large-scale image recognition. *arXiv preprint arXiv:1409.1556*.
- Tan, C., Yang, M., You, Z., Chen, H., Zhang, Y., 2022. A selective kernel-based cycle-consistent generative adversarial network for unpaired low-dose CT denoising. *Precision Clinical Medicine* 5, pbac011.
- Tronchin, L., Sicilia, R., Cordelli, E., Ramella, S., Soda, P., 2021. Evaluating GANs in medical imaging, in: *Deep Generative Models, and Data Augmentation, Labelling, and Imperfections: First Workshop, MICCAI 2021, Proceedings*, Springer. pp. 112–121.
- Venkatanath, N., Praneeth, D., Bh, M.C., Channappayya, S.S., Medasani, S.S., 2015. Blind image quality evaluation using perception based features, in: *2015 twenty first national conference on communications (NCC)*, IEEE. pp. 1–6.
- Vision and I. A. Group, 2009. VIA/I-ELCAP public access research database. <http://www.via.cornell.edu/databases/lungdb.html>. Accessed April 7, 2009.
- Wang, Z., Bovik, A.C., Sheikh, H.R., Simoncelli, E.P., 2004. Image quality assessment: from error visibility to structural similarity. *IEEE transactions on image processing* 13, 600–612.
- Wolterink, J.M., Leiner, T., Viergever, M.A., Išgum, I., 2017. Generative adversarial networks for noise reduction in low-dose CT. *IEEE transactions on medical imaging* 36, 2536–2545.
- Yang, L., Liu, H., Shang, F., Liu, Y., 2023. Adaptive Non-Local Generative Adversarial Networks for Low-Dose CT Image Denoising, in: *ICASSP 2023-2023 IEEE International Conference on Acoustics, Speech and Signal Processing (ICASSP)*, IEEE. pp. 1–5.
- Yang, Q., Yan, P., Zhang, Y., Yu, H., Shi, Y., Mou, X., Kalra, M.K., Zhang, Y., Sun, L., Wang, G., 2018. Low-dose CT image denoising using a generative adversarial network with Wasserstein distance and perceptual loss. *IEEE transactions on medical imaging* 37, 1348–1357.
- Yin, Z., Xia, K., He, Z., Zhang, J., Wang, S., Zu, B., 2021. Unpaired image denoising via Wasserstein GAN in low-dose CT image with multi-perceptual loss and fidelity loss. *Symmetry* 13, 126.

- Yin, Z., Xia, K., Wang, S., He, Z., Zhang, J., Zu, B., 2023. Unpaired low-dose CT denoising via an improved cycle-consistent adversarial network with attention ensemble. *The Visual Computer* 39, 4423–4444.
- You, C., Yang, Q., Shan, H., Gjesteb, L., Li, G., Ju, S., Zhang, Z., Zhao, Z., Zhang, Y., Cong, W., Weng, 2018. Structurally-sensitive multi-scale deep neural network for low-dose CT denoising. *IEEE access* 6, 41839–41855.
- Zamir, S.W., Arora, A., Khan, S., Hayat, M., Khan, F.S., Yang, M.H., Shao, L., 2021. Multi-stage progressive image restoration, in: *Proceedings of the IEEE/CVF conference on computer vision and pattern recognition*, pp. 14821–14831.
- Zhang, H., Goodfellow, I., Metaxas, D., Odena, A., 2019. Self-attention generative adversarial networks, in: *International conference on machine learning*, PMLR. pp. 7354–7363.
- Zhao, H., Gallo, O., Frosio, I., Kautz, J., 2016. Loss functions for image restoration with neural networks. *IEEE Transactions on computational imaging* 3, 47–57.
- Zhu, J.Y., Park, T., Isola, P., Efros, A.A., 2017. Unpaired image-to-image translation using cycle-consistent adversarial networks, in: *Proceedings of the IEEE international conference on computer vision*, pp. 2223–2232.

Supplementary material

Multi-Scale Texture Loss for CT Denoising with GANs

Francesco Di Feola^a, Lorenzo Tronchin^b, Valerio Guarrasi^b, Paolo Soda^{a, b}

^a*Department of Diagnostics and Intervention, Radiation Physics, Biomedical Engineering, Umeå University, Sweden*

^b*Unit of Computer Systems and Bioinformatics, Department of Engineering, University Campus Bio-Medico of Rome, Italy*

1. Introduction

This document provides supplementary material to the main manuscript, providing a detailed description of the GAN backbones used, figures, and tables, there omitted for readability. In detail, this document is organized as follows: section 2 reports a description of the GAN backbones used, providing information about their architectures as well as the computation of their loss function; section 3 presents visual results attained using CycleGAN, Pix2Pix and UNIT across various configurations of the loss function; section 4 provides the list of patient IDs across all the datasets described in the main manuscript; section 5 presents statistical analysis performed on a per-patient basis.

2. Deep Models

This section describes the GAN architectures used in this work. Let us remember that $\mathbf{x} \in X$ is a LDCT image, whilst $\mathbf{y} \in Y$ is an HDCT image.

2.0.1. Pix2Pix

Pix2Pix is a well-established baseline for image-to-image translation tasks (?). Based on conditional GAN (cGAN), Pix2Pix requires pairs of images in the training phase, restricting its application to paired datasets. It uses a generator G and a discriminator D which, in the original paper (?), are implemented as a U-Net encoder-decoder architecture and a PatchGAN, respectively. The loss function of a cGAN is the adversarial loss:

$$\mathcal{L}_{cGAN}(G, D) = \mathbb{E}_{\mathbf{x}, \mathbf{y}}[\log D(\mathbf{x}, \mathbf{y})] + \mathbb{E}_{\mathbf{x}, \mathbf{z}}[\log(1 - D(G(\mathbf{x}, \mathbf{z})))] \quad (1)$$

where G and D are trained in an alternating fashion performing a min-max optimization, \mathbb{E} is the expectation operator, and \mathbf{z} is a Gaussian noise vector that in (?) is provided in the form of dropout applied on the layers of G . In Pix2Pix, the goal of the generator is not only to fool the discriminator but also to generate $G(\mathbf{x}, \mathbf{z}) \approx \mathbf{y}$.

To this end, a pixel-wise regression loss is used:

$$\mathcal{L}_{L1}(G) = \mathbb{E}_{\mathbf{x}, \mathbf{y}, \mathbf{z}}[\|\mathbf{y} - G(\mathbf{x}, \mathbf{z})\|_1] \quad (2)$$

where $\|\cdot\|_1$ is the L-1 distance. The final objective function of Pix2Pix is:

$$\mathcal{L} = \mathcal{L}_{cGAN} + \lambda \mathcal{L}_1 \quad (3)$$

where λ is a weighting parameter that is empirically set to 1 (?).

2.0.2. CycleGAN

Paired translation is not very practical and feasible, especially in the medical domain where the acquisition of paired datasets may be complex. For this reason, unpaired methods have attracted more attention and CycleGAN established itself as a milestone architecture. Being a bidirectional generative model that contains two generators (G, F) and two discriminators (D_X, D_Y), CycleGAN tackles unpaired translation introducing the cycle-consistency constraint which attempts to regularize and reduce the space of possible mappings (?), helping G and F to be bijective functions. In the original paper (?), G and F are implemented as residual encoder-decoder architectures, whilst D_X and D_Y are implemented as PatchGANs. CycleGAN applies least squares adversarial losses to both generators. For the generator G and the discriminator D_Y the adversarial loss is expressed as:

$$\mathcal{L}_{LSGAN}(G, D_Y, X, Y) = \mathbb{E}_{\mathbf{y}}[(D_Y(\mathbf{y}) - 1)^2] + \mathbb{E}_{\mathbf{x}}[(D_Y(G(\mathbf{x})) - 1)^2]. \quad (4)$$

A similar adversarial loss is introduced for the generator F and the discriminator D_X .

The cycle consistency constraint is implemented as a loss term called cycle consistency loss:

$$\mathcal{L}_{cyc}(G, F) = \mathbb{E}_{\mathbf{x}}[\|F(G(\mathbf{x})) - \mathbf{x}\|_1] + \mathbb{E}_{\mathbf{y}}[\|G(F(\mathbf{y})) - \mathbf{y}\|_1] \quad (5)$$

which encourages $F(G(\mathbf{x})) = \tilde{\mathbf{x}} \approx \mathbf{x}$ and $G(F(\mathbf{y})) = \tilde{\mathbf{y}} \approx \mathbf{y}$, i.e., it imposes latent space constraints to encourage the information content to be preserved during the reconstruction mapping.

Similarly to the cycle consistency loss, an identity loss function is introduced to further regularize the mapping behavior of the generators:

$$\mathcal{L}_{idt}(G, F) = \mathbb{E}_{\mathbf{x}}[\|F(\mathbf{x}) - \mathbf{x}\|_1] + \mathbb{E}_{\mathbf{y}}[\|G(\mathbf{y}) - \mathbf{y}\|_1]. \quad (6)$$

The final objective function of CycleGAN is:

$$\mathcal{L} = \mathcal{L}_{SGAN} + \lambda_1 \mathcal{L}_{cyc} + \lambda_2 \mathcal{L}_{idt} \quad (7)$$

where the weighting parameters λ_1 and λ_2 are empirically set to 10 and 0.5 (?), respectively.

2.0.3. UNIT

UNIT (Unsupervised Image-to-Image-Translation) tackles unpaired scenarios by assuming that a pair of corresponding images in different domains can be mapped to the same representation in a shared latent space (?). UNIT is composed of six sub-networks: two encoders E_X, E_Y that map the input to a shared latent representation, two decoders G_X, G_Y that reconstruct the translated output and two discriminators D_X and D_Y . In the original paper (?), E_X, E_Y, G_X, G_Y share the same structure consisting of 3 convolutional layers and 4 basic residual blocks, whilst D_X, D_Y are implemented as PatchGANs. The optimization problem is solved by interpreting the roles of the six subnetworks as follows: the encoder-decoder pairs $\{E_X, G_X\}$ and $\{E_Y, G_Y\}$ constitute two variational autoencoders referred as VAE_X and VAE_Y , whilst $\{G_X, D_X\}$ and $\{G_Y, D_Y\}$ are two GANs referred as GAN_X and GAN_Y .

The adversarial losses are:

$$\mathcal{L}_{GAN_X}(E_Y, G_X, D_X) = \lambda_0 \mathbb{E}_{\mathbf{x}}[\log D_X(\mathbf{x})] + \lambda_0 \mathbb{E}_{\mathbf{z}_Y}[\log(1 - D_X(G_X(\mathbf{z}_Y)))] \quad (8)$$

$$\mathcal{L}_{GAN_Y}(E_X, G_Y, D_Y) = \lambda_0 \mathbb{E}_{\mathbf{y}}[\log D_Y(\mathbf{y})] + \lambda_0 \mathbb{E}_{\mathbf{z}_X}[\log(1 - D_Y(G_Y(\mathbf{z}_X)))] \quad (9)$$

where \mathbf{z}_X and \mathbf{z}_Y are the latent representations produced by the two encoders E_X and E_Y , respectively.

VAE_X and VAE_Y are trained to minimize a variational upper bound with their loss function defined as:

$$\mathcal{L}_{VAE_X}(E_X, G_X) = \lambda_1 KL(q_X(\mathbf{z}_X|\mathbf{x})||p_\eta(\mathbf{z})) - \lambda_2 \mathbb{E}_{\mathbf{z}_X}[\log(p_{G_X}(\mathbf{x}|\mathbf{z}_X))] \quad (10)$$

$$\mathcal{L}_{VAE_Y}(E_Y, G_Y) = \lambda_1 KL(q_Y(\mathbf{z}_Y|\mathbf{y})||p_\eta(\mathbf{z})) - \lambda_2 \mathbb{E}_{\mathbf{z}_Y}[\log(p_{G_Y}(\mathbf{y}|\mathbf{z}_Y))] \quad (11)$$

where KL is the Kullback Leibler divergence that penalizes deviation of the distribution of the latent codes $q_1(\mathbf{z}_X|\mathbf{x})$, $q_2(\mathbf{z}_Y|\mathbf{y})$ from the prior distribution $p_\eta(\mathbf{z})$, whilst $p_{G_X}(\mathbf{x}|\mathbf{z}_X)$ and $p_{G_Y}(\mathbf{y}|\mathbf{z}_Y)$ are distributions of the reconstructed samples starting from the latent codes \mathbf{z}_X , \mathbf{z}_Y . On a practical level, the negative likelihood can be replaced with the L_1 distance computed between an image and its reconstruction, i.e., $\|\mathbf{x} - G_X(\mathbf{z}_X)\|_1$ or $\|\mathbf{y} - G_Y(\mathbf{z}_Y)\|_1$. The weights λ_1 , λ_2 are set to default values, 0.1 and 100, respectively.

A similar term is used to model the cycle-consistency constraint, given by:

$$\begin{aligned} \mathcal{L}_{cy_{cX}}(E_X, G_X, E_Y, G_Y) = & \lambda_3 KL(q_X(\hat{\mathbf{z}}_X|\mathbf{x})||p_\eta(\mathbf{z})) + \lambda_3 KL(q_Y(\hat{\mathbf{z}}_Y|\hat{\mathbf{y}})||p_\eta(\mathbf{z})) + \\ & - \lambda_4 \mathbb{E}_{\hat{\mathbf{z}}_Y}[\log(p_{G_X}(\mathbf{x}|\hat{\mathbf{z}}_Y))] \end{aligned} \quad (12)$$

$$\begin{aligned} \mathcal{L}_{cy_{cY}}(E_Y, G_Y, E_X, G_X) = & \lambda_3 KL(q_Y(\hat{\mathbf{z}}_Y|\mathbf{y})||p_\eta(\mathbf{z})) + \lambda_3 KL(q_X(\hat{\mathbf{z}}_X|\hat{\mathbf{x}})||p_\eta(\mathbf{z})) + \\ & - \lambda_4 \mathbb{E}_{\hat{\mathbf{z}}_X}[\log(p_{G_Y}(\mathbf{y}|\hat{\mathbf{z}}_X))] \end{aligned} \quad (13)$$

where the KL terms penalize the latent codes $q_X(\mathbf{z}_X|\mathbf{x})$, $q_Y(\mathbf{z}_Y|\hat{\mathbf{y}})$, $q_Y(\mathbf{z}_Y|\mathbf{y})$ and $q_X(\mathbf{z}_X|\hat{\mathbf{x}})$ deviating from the prior distribution $p_\eta(\mathbf{z})$. The generated samples are $\hat{\mathbf{x}} = G_X(\mathbf{z}_Y)$ and $\hat{\mathbf{y}} = G_Y(\mathbf{z}_X)$ whilst $\hat{\mathbf{z}}_X = E_X(\hat{\mathbf{x}})$ and $\hat{\mathbf{z}}_Y = E_Y(\hat{\mathbf{y}})$ are latent representations. Also here, the negative log-likelihoods can be expressed in terms of L1-distances, i.e., $\|\mathbf{x} - G_X(\hat{\mathbf{z}}_X)\|_1$ and $\|\mathbf{y} - G_Y(\hat{\mathbf{z}}_Y)\|_1$ where $G_X(\hat{\mathbf{z}}_X) = \tilde{\mathbf{x}}$ and $G_Y(\hat{\mathbf{z}}_Y) = \tilde{\mathbf{y}}$. The weights of each loss term are set to default values with $\lambda_0 = 10$, $\lambda_1 = \lambda_3 = 0.1$ and $\lambda_2 = \lambda_4 = 100$.

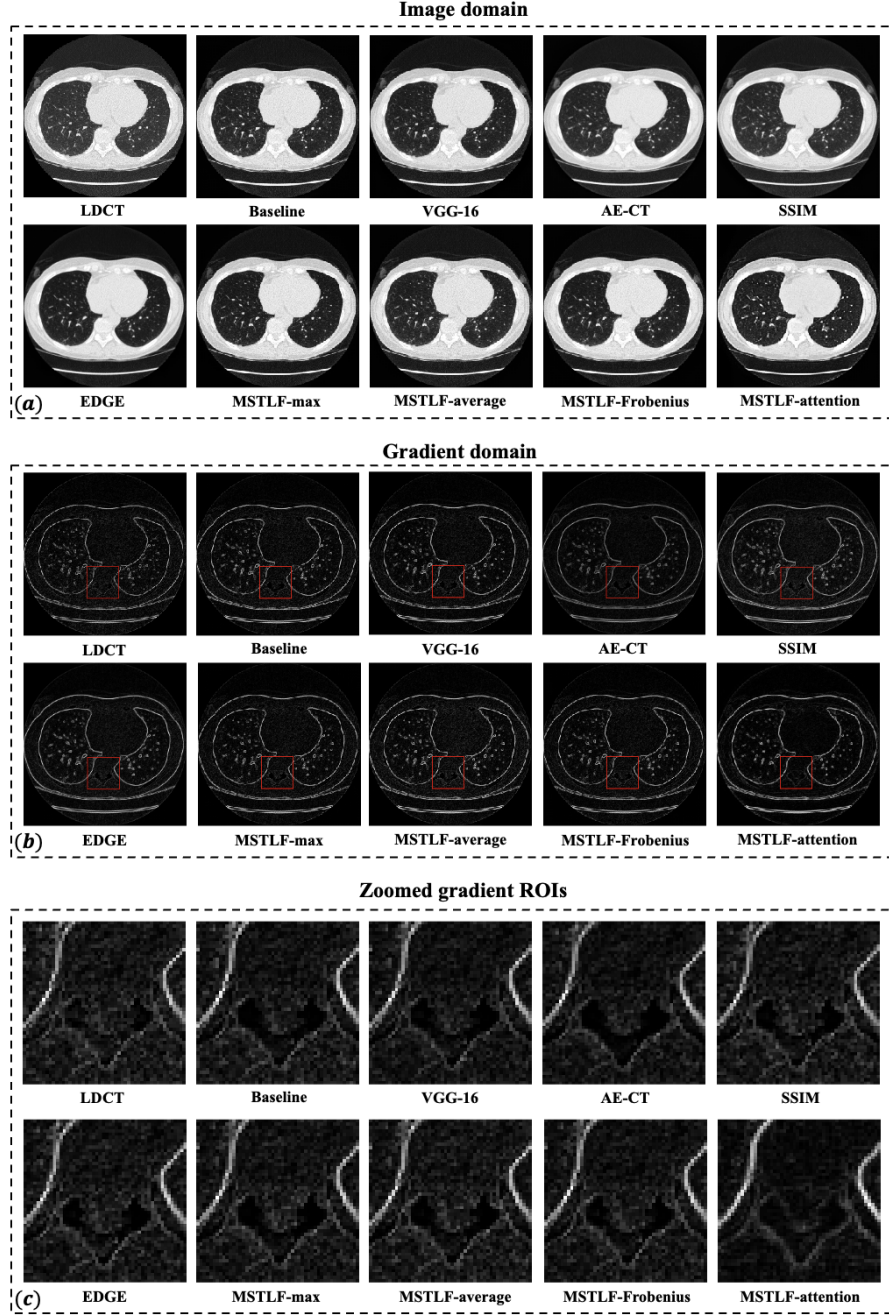
The final objective function of UNIT is computed as:

$$\mathcal{L} = \mathcal{L}_{VAE} + \mathcal{L}_{GAN} + \mathcal{L}_{cyc}. \quad (14)$$

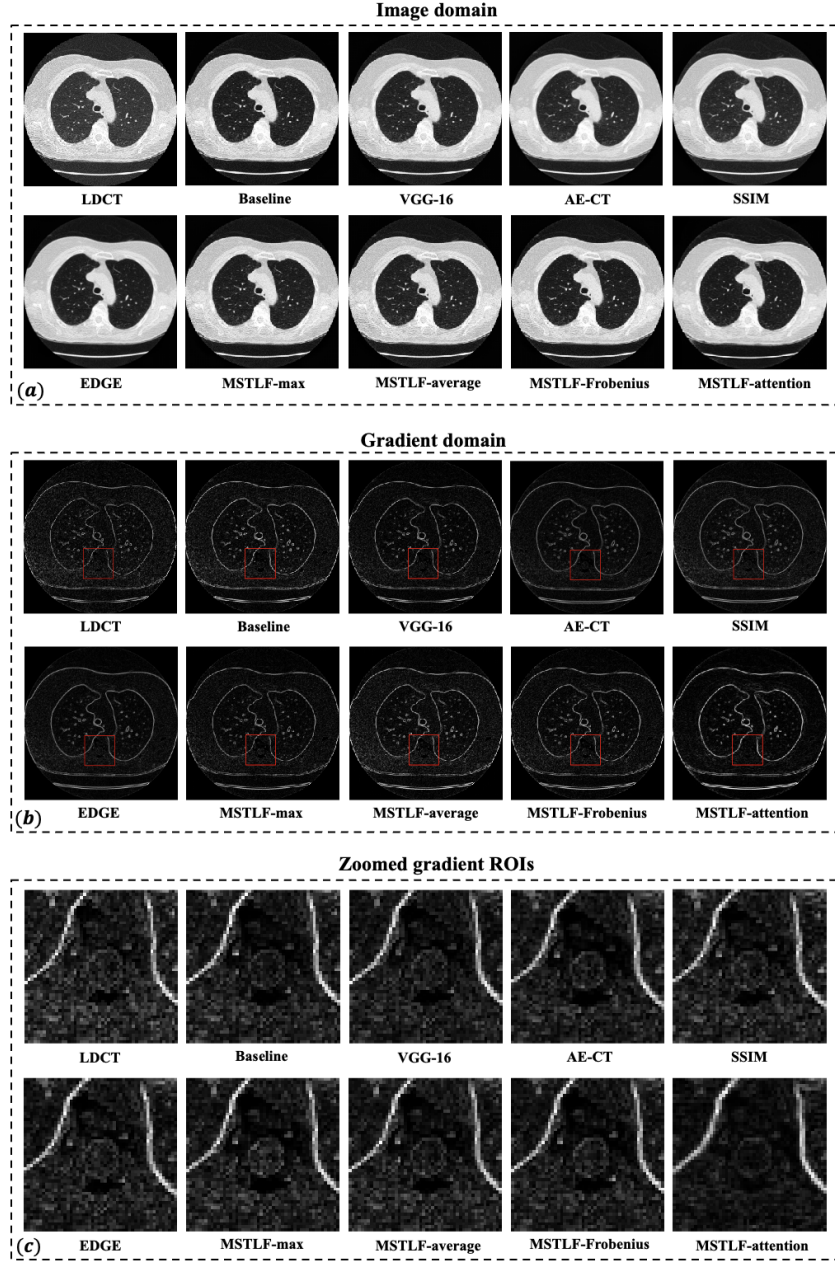
3. Visual results

This section presents visual results attained using CycleGAN, Pix2Pix, and UNIT across different configurations of the loss function and different datasets. Each figure is structured as follows: panel (a) reports images in the image domain, panel (b) shows the same images in the gradient domain and panel (c) shows the zoomed Regions Of Interest (ROIs) identified by the red boxes in the gradient images, which contain areas inside and outside the lung regions, thus including different tissues and anatomical structures. Supplementary Figure 1 and 2 depict examples of denoised images obtained using CycleGAN applied to *Dataset B* (LIDC/IDRI dataset) and *Dataset C* (ELCAP dataset), respectively. Supplementary Figure 3, 4, and 5 show examples of denoised images obtained through Pix2Pix on *Dataset A* (Mayo simulated data), *Dataset B* (LIDC/IDRI dataset), and *Dataset C* (ELCAP dataset), respectively. Furthermore, Supplementary Figure 6, 7, and 8 show examples

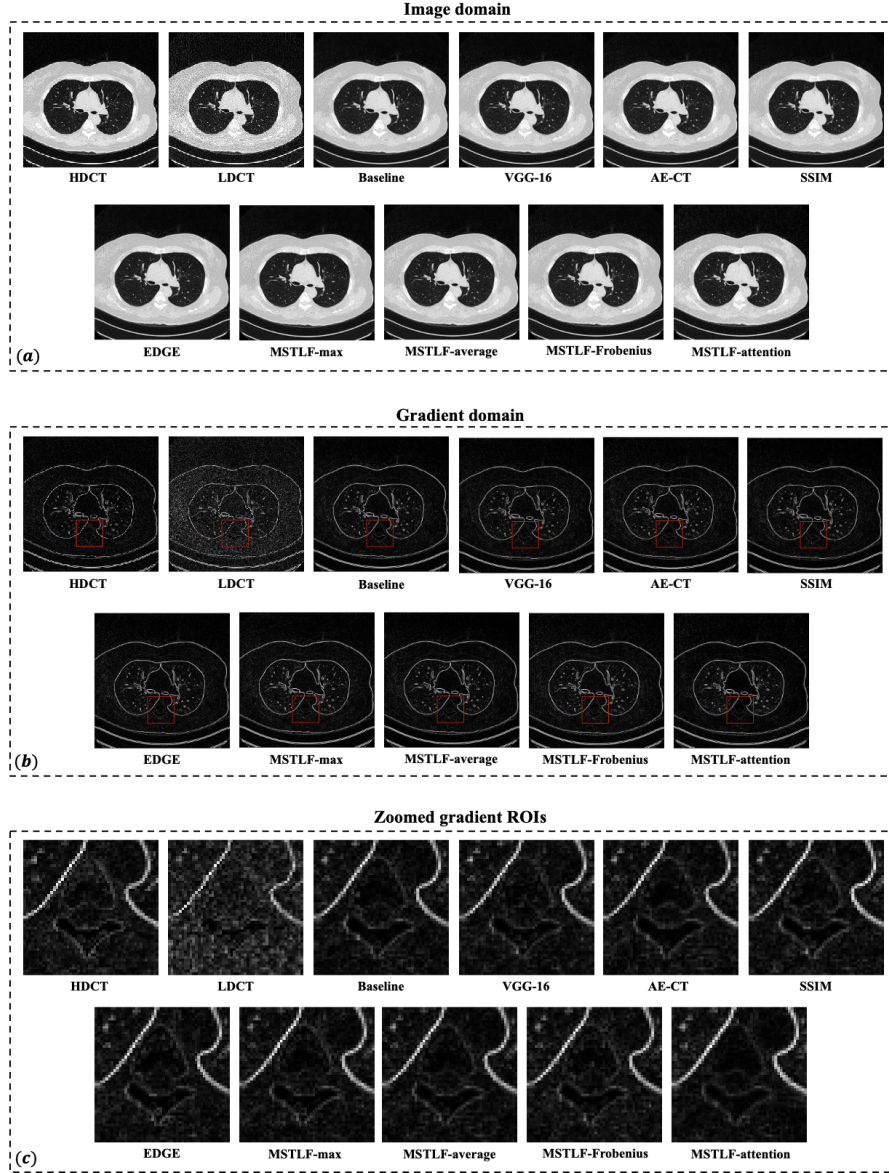
of denoised images produced by UNIT on *Dataset A* (Mayo simulated data), *Dataset B* (LIDC/IDRI dataset), and *Dataset C* (ELCAP dataset), respectively. As mentioned in the main manuscript, MSTLF-attention produced the image with the lowest gradient that, in turn, corresponds to the lowest level of noise while preserving the lung boundaries, as shown in Supplementary Figure 1, 2, 3, 4, 5, 6, 7, 8 (c).



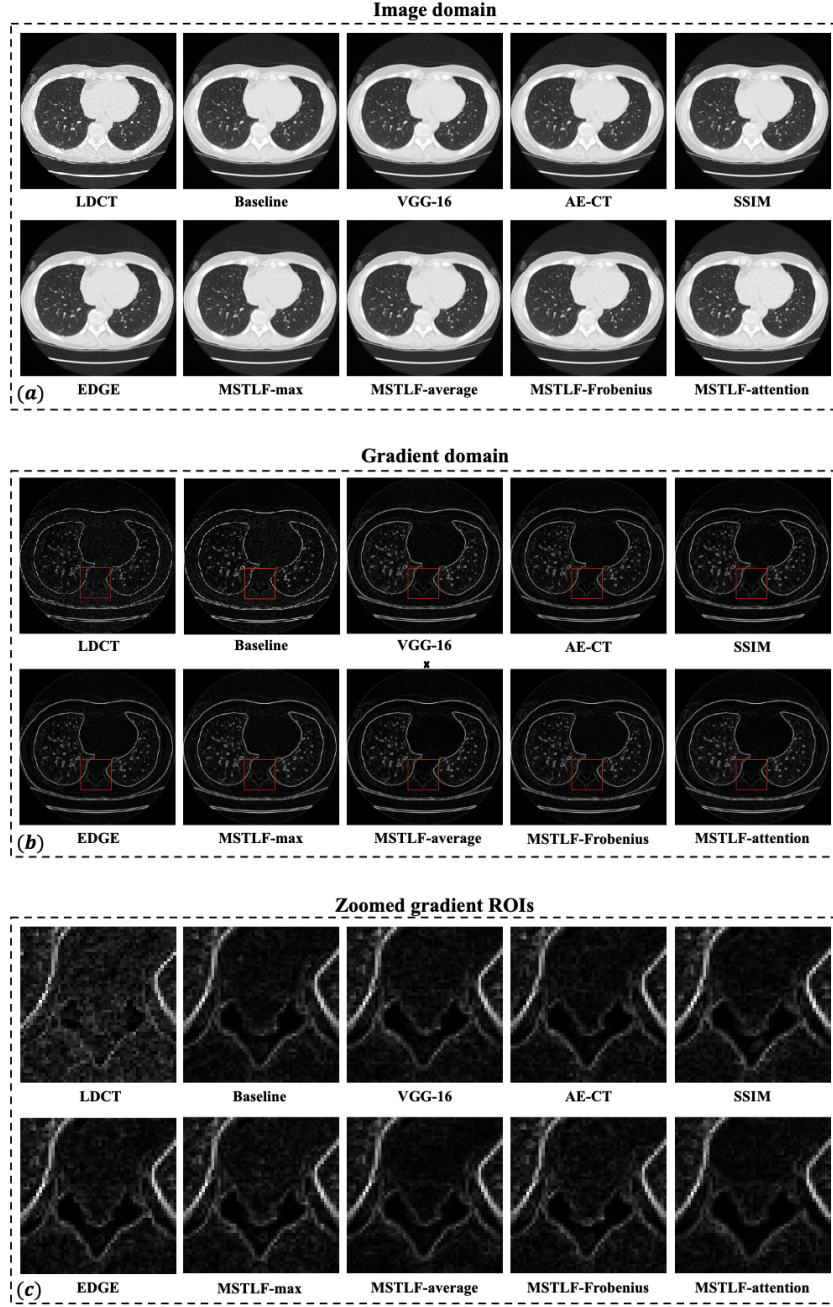
Supplementary Figure 1: Visual comparison of denoised CT slices from the LIDC/IDRI dataset (*Dataset B*). We show all loss function configurations for CycleGAN. The images are shown both in the image domain (panel (a) using a display window in $[-1200, 200]$ HU), and the gradient domain (panel (b)). The zoomed ROI in panel (c) highlights denoising in the gradient domain.



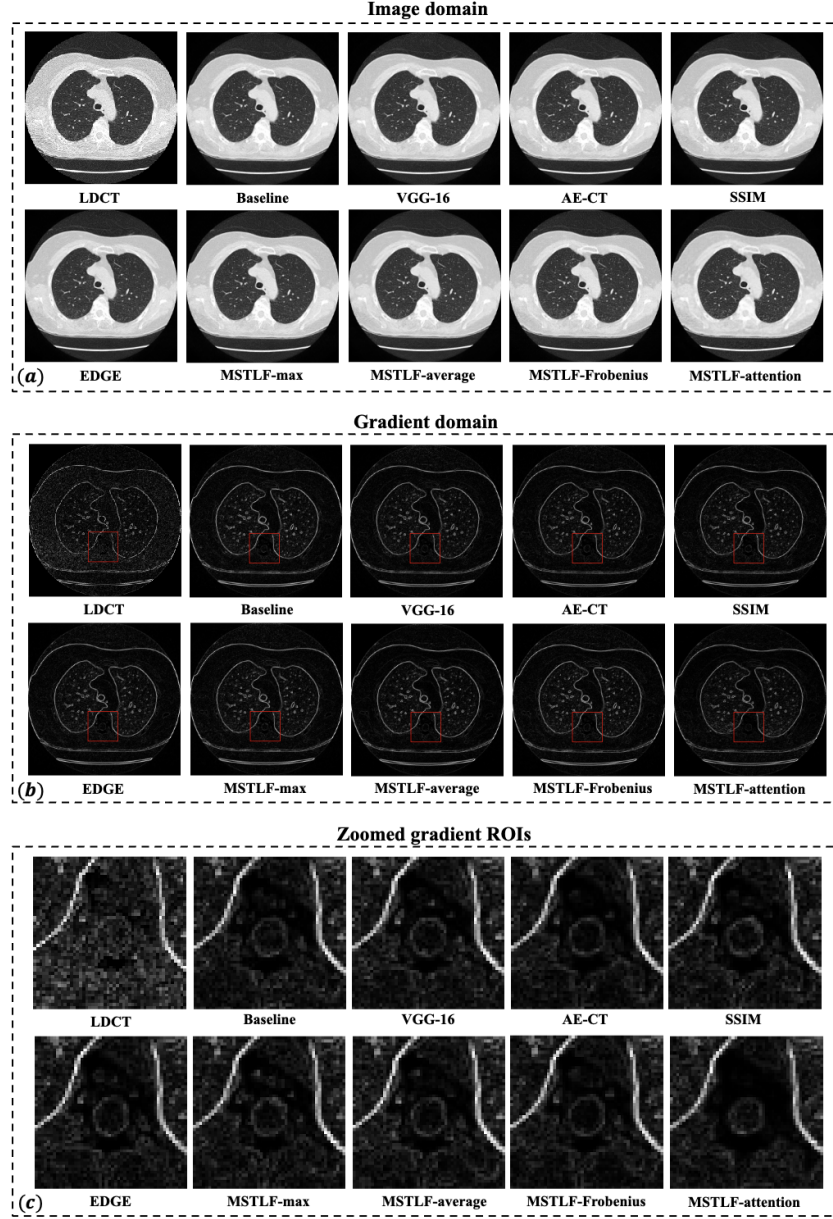
Supplementary Figure 2: Visual comparison of denoised CT slices the ELCAP dataset (*Dataset C*). We show all loss function configurations for CycleGAN. The images are shown both in the image domain (panel (a) using a display window in $[-1200, 200]$ HU), and the gradient domain (panel (b)). The zoomed ROI in panel (c) highlights denoising in the gradient domain.



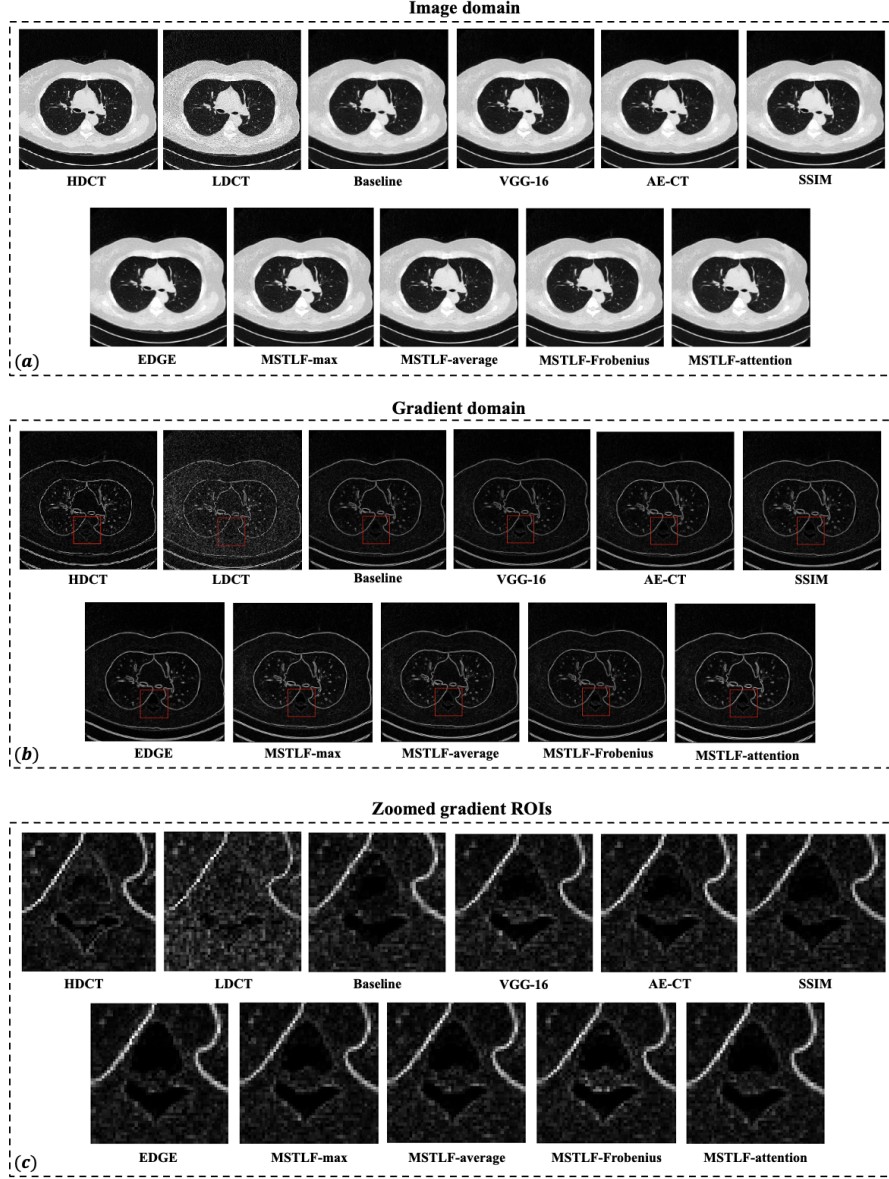
Supplementary Figure 3: Visual comparison of denoised CT slices from the Mayo Clinic simulated data (*Dataset A*). We show all loss function configurations for Pix2Pix. The images are shown both in the image domain (panel (a) using a display window in $[-1200, 200]$ HU), and the gradient domain (panel (b)). The zoomed ROI in panel (c) highlights denoising in the gradient domain.



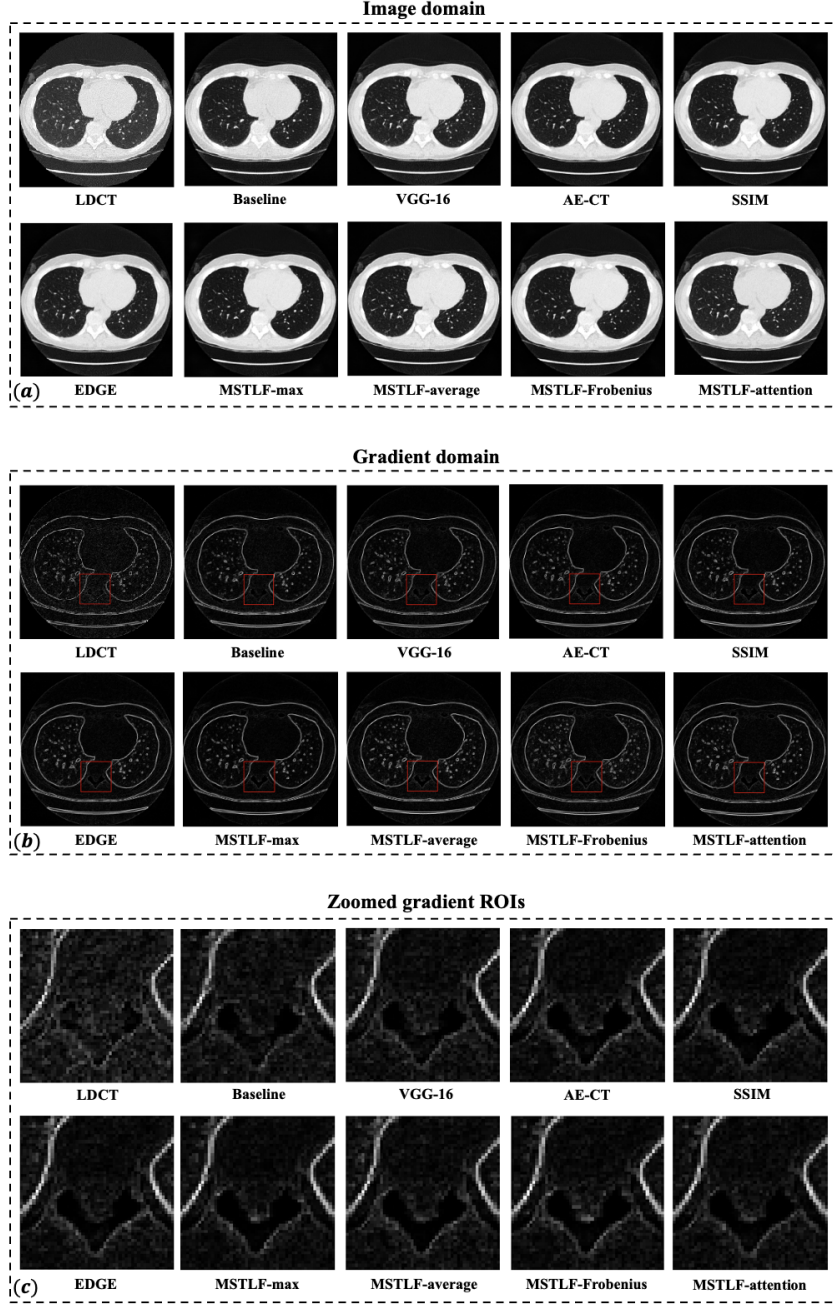
Supplementary Figure 4: Visual comparison of denoised CT slices from the LIDC/IDRI dataset (*Dataset B*). We show all loss function configurations for Pix2Pix. The images are shown both in the image domain (panel (a)) using a display window in $[-1200, 200]$ HU), and the gradient domain (panel (b)). The zoomed ROI in panel (c) highlights denoising in the gradient domain.



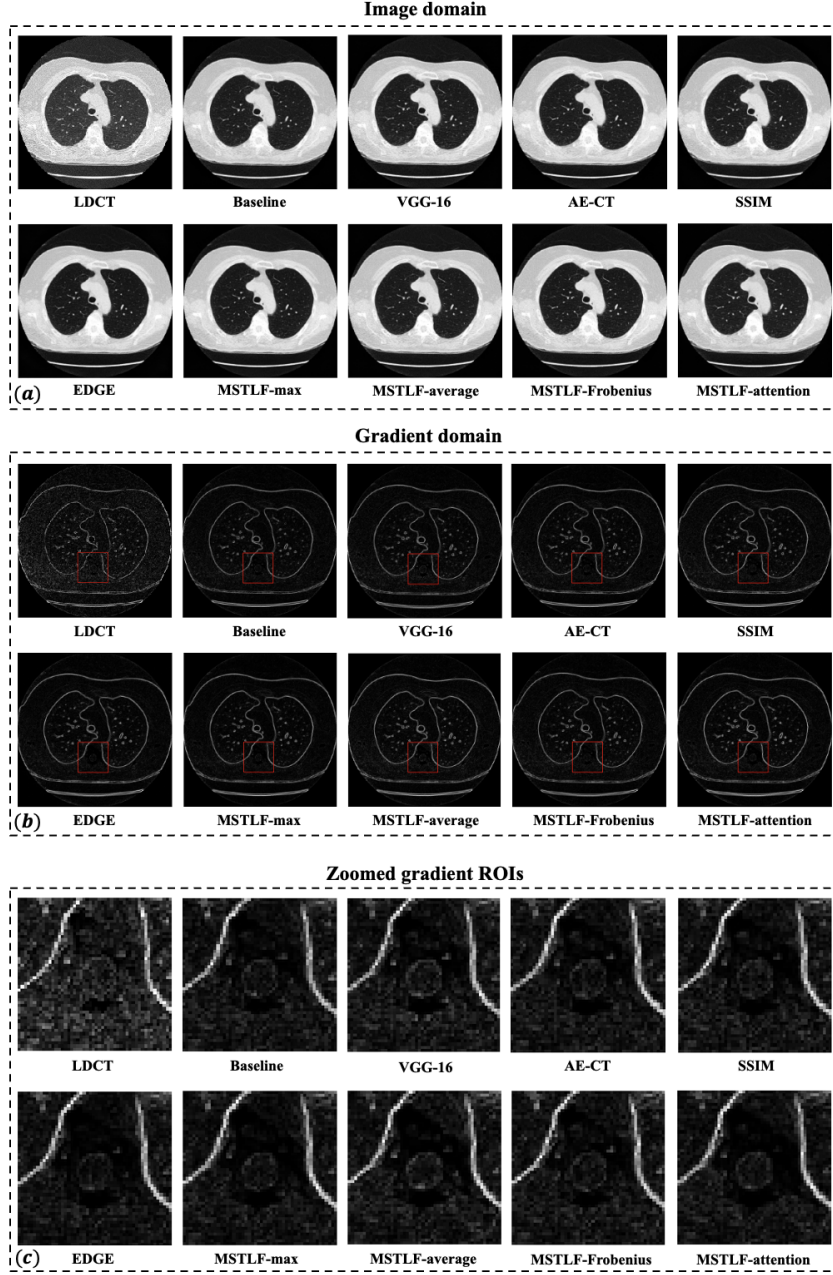
Supplementary Figure 5: Visual comparison of denoised CT slices from the ELCAP dataset (*Dataset C*). We show all loss function configurations for Pix2Pix. The images are shown both in the image domain (panel (a) using a display window in $[-1200, 200]$ HU), and the gradient domain (panel (b)). The zoomed ROI in panel (c) highlights denoising in the gradient domain.



Supplementary Figure 6: Visual comparison of denoised CT slices from the Mayo Clinic simulated data (*Dataset A*). We show all loss function configurations for UNIT. The images are shown both in the image domain (panel (a)) using a display window in $[-1200, 200]$ HU), and the gradient domain (panel (b)). The zoomed ROI in panel (c) highlights denoising in the gradient domain.



Supplementary Figure 7: Visual comparison of denoised CT slices from the LIDC/IDRI dataset (*Dataset B*). We show all loss function configurations for UNIT. The images are shown both in the image domain (panel (a)) using a display window in $[-1200, 200]$ HU), and the gradient domain (panel (b)). The zoomed ROI in panel (c) highlights denoising in the gradient domain.



Supplementary Figure 8: Visual comparison of denoised CT slices from the ELCAP dataset (*Dataset C*). We show all loss function configurations for UNIT. The images are shown both in the image domain (panel (a) using a display window in $[-1200, 200]$ HU), and the gradient domain (panel (b)). The zoomed ROI in panel (c) highlights denoising in the gradient domain.

4. Patients' IDs

LDCT-and-Projection Data by Mayo Clinic (?):

- Training set: L096, L109, L143, L192, L286, L291, L310, L333, L506;
- Test set (referred to as *Dataset A* in this manuscript): L067, C002, C004, C030, C067, C120, C124, C166;

LIDC/IDRI (referred to as *Dataset B* in this manuscript) (?):

0361, 0369, 0555, 0574, 0785, 0928, 0930, 0959.

ELCAP dataset (referred to as *Dataset C* in this manuscript) (?): W0001, W0002, W0003, W0004, W0005, W0006, W0007, W0008, W0009, W0010, W0011, W0012, W0013, W0014, W0015, W0016, W0017, W0018, W0019, W0020, W0021, W0022, W0023, W0024, W0025, W0026, W0027, W0028, W0029, W0030, W0031, W0032, W0033, W0034, W0035, W0036, W0037, W0038, W0039, W0040, W0041, W0042, W0043, W0044, W0045, W0046, W0047, W0048, W0049, W0050.

5. Statistical analysis

This section presents the statistical analysis conducted on an individual patient basis. We evaluate the statistical significance of the best-performing loss function configuration compared to other configurations using the Wilcoxon signed rank test, with a p-value threshold set at $p \leq 0.05$. The main manuscript demonstrates that MSTLF attains the best overall performance across different datasets and GAN architectures. In particular, MSTLF-average yields the most favorable results on paired metrics (PSNR, MSE, and SSIM), whilst MSTLF-attention excels in unpaired metrics (NIQE and PIQUE).

Hereinafter, the tables share the same structure reporting the following information: the dataset used (first row), GAN architecture and performance metrics (second row), the configuration of the loss function whose statistical significance is assessed against the other configurations (first and second columns, respectively). For each comparison, the tables report the number of patients for whom the loss function in the first column is statistically better than the loss function in the second column. The second-to-last row and column sum up the values to summarize the results across metrics and loss functions configurations, while the last row and column show the percentage.

The per-patient analysis offers additional insights into the findings presented in the main manuscript, confirming the results attained. In particular, Supplementary Table 1-12 corroborate the results reported in Tables 3 and 4 of the main document. It is worth noting that although we showed the agnosticism of the proposed MSTLF with respect to the GAN architecture used, the per-patient analysis brings out that among the three architectures, cycleGAN is the one with the largest percentage in the last column (Supplementary Table 2, 5, 8, 11).

<i>Dataset A</i>						
Pix2Pix		PNSR	MSE	SSIM	Total	%
MSTLF-average vs	Baseline	8	6	8	22/24	92%
	VGG-16	8	7	8	23/24	96%
	AE-CT	6	7	6	19/24	79%
	SSIM-L	3	6	0	9/24	38%
	EDGE	6	7	8	21/24	88%
	MSTLF-max	8	8	8	24/24	100%
	MSTLF-Frobenius	8	8	7	23/24	96%
	MSTLF-attention	8	8	8	24/24	100%
	Total	55/64	57/64	53/64		
	%	86%	89%	83%		

Supplementary Table 1: Wilcoxon signed rank test conducted on a per patient basis within *Dataset A* (Mayo simulated data, 8 patients in total) to assess the statistical significance of MSTLF-average in comparison to other loss function configurations, with the Pix2Pix. Each box shows the number of patients for whom MSTLF-average is statistically better than other loss functions.

<i>Dataset A</i>						
CycleGAN		PNSR	MSE	SSIM	Total	%
MSTLF-average vs	Baseline	8	8	8	24/24	100%
	VGG-16	7	7	6	20/24	83%
	AE-CT	4	4	7	15/24	63%
	SSIM-L	8	8	8	24/24	100%
	EDGE	8	8	8	24/24	100%
	MSTLF-max	7	7	7	21/24	88%
	MSTLF-Frobenius	6	6	6	18/24	75%
	MSTLF-attention	7	7	6	20/24	83%
	Total	55/64	57/64	56/64		
	%	86%	86%	88%		

Supplementary Table 2: Wilcoxon signed rank test conducted on a per patient basis within *Dataset A* (Mayo simulated data, 8 patients in total) to assess the statistical significance of MSTLF-average in comparison to other loss function configurations in CycleGAN. Each box shows the number of patients for whom MSTLF-average is statistically better.

<i>Dataset A</i>						
UNIT		PNSR	MSE	SSIM	Total	%
MSTLF-average vs	Baseline	8	8	8	24/24	100%
	VGG-16	8	8	8	24/24	100%
	AE-CT	8	8	8	24/24	100%
	SSIM-L	7	7	8	22/24	92%
	EDGE	8	8	8	24/24	100%
	MSTLF-max	8	8	8	24/24	100%
	MSTLF-Frobenius	8	8	8	24/24	100%
	MSTLF-attention	6	5	8	19/24	79%
	Total	61/64	60/64	64/64		
	%	92%	94%	100%		

Supplementary Table 3: Wilcoxon signed rank test conducted on a per patient basis within *Dataset A* (Mayo simulated data, 8 patients in total) to assess the statistical significance of MSTLF-average in comparison to other loss function configurations in UNIT. Each box shows the number of patients for whom MSTLF-average is statistically better.

<i>Dataset A</i>					
Pix2Pix		NIQE	PIQUE	Total	%
MSTLF-attention vs	Baseline	8	7	15/16	94%
	VGG-16	8	7	15/16	94%
	AE-CT	8	7	15/16	94%
	SSIM-L	8	7	15/16	94%
	EDGE	8	7	15/16	94%
	MSTLF-max	8	7	15/16	94%
	MSTLF-average	8	7	15/16	94%
	MSTLF-Frobenius	8	7	15/16	94%
	Total	64/64	56/64		
	%	100%	88%		

Supplementary Table 4: Wilcoxon signed rank test conducted on a per patient basis within *Dataset A* (Mayo simulated data, 8 patients in total) to assess the statistical significance of MSTLF-attention in comparison to other loss function configurations in Pix2Pix. Each box shows the number of patients for whom MSTLF-attention is statistically better.

<i>Dataset A</i>					
CycleGAN		NIQE	PIQUE	Total	%
MSTLF-attention vs	Baseline	8	8	16/16	100%
	VGG-16	8	8	16/16	100%
	AE-CT	8	8	16/16	100%
	SSIM-L	8	8	16/16	100%
	EDGE	8	8	16/16	100%
	MSTLF-max	8	8	16/16	100%
	MSTLF-average	8	8	16/16	100%
	MSTLF-Frobenius	8	8	16/16	100%
	Total	64/64	64/64		
	%	100%	100%		

Supplementary Table 5: Wilcoxon signed rank test conducted on a per patient basis within *Dataset A* (Mayo simulated data, 8 patients in total) to assess the statistical significance of MSTLF-attention in comparison to other loss function configurations in CycleGAN. Each box shows the number of patients for whom MSTLF-attention is statistically better.

<i>Dataset A</i>					
UNIT		NIQE	PIQUE	Total	%
MSTLF-attention vs	Baseline	8	8	16/16	100%
	VGG-16	8	8	16/16	100%
	AE-CT	7	7	14/16	88%
	SSIM-L	7	7	14/16	88%
	EDGE	7	7	14/16	88%
	MSTLF-max	8	8	16/16	100%
	MSTLF-average	8	8	16/16	100%
	MSTLF-Frobenius	8	8	16/16	100%
	Total	61/64	61/64		
	%	95%	95%		

Supplementary Table 6: Wilcoxon signed rank test conducted on a per patient basis within *Dataset A* (Mayo simulated data, 8 patients in total) to assess the statistical significance of MSTLF-attention in comparison to other loss function configurations in UNIT. Each box shows the number of patients for whom MSTLF-attention is statistically better.

<i>Dataset B</i>					
Pix2Pix		NIQE	PIQUE	Total	%
MSTLF-attention vs	Baseline	8	8	16/16	100%
	VGG-16	7	8	15/16	94%
	AE-CT	5	5	10/16	63%
	SSIM-L	5	6	11/16	69%
	EDGE	7	8	15/16	94%
	MSTLF-max	7	8	15/16	94%
	MSTLF-average	6	7	13/16	81%
	MSTLF-Frobenius	6	6	12/16	75%
	Total	51/64	56/64		
	%	80%	88%		

Supplementary Table 7: Wilcoxon signed rank test conducted on a per patient basis within *Dataset B* (LIDC/IDRI dataset, 8 patients in total) to assess the statistical significance of MSTLF-attention in comparison to other loss function configurations in Pix2Pix. Each box shows the number of patients for whom MSTLF-attention is statistically better.

<i>Dataset B</i>					
cycleGAN		NIQE	PIQUE	Total	%
MSTLF-attention vs	Baseline	8	8	16/16	100%
	VGG-16	8	8	16/16	100%
	AE-CT	8	8	16/16	100%
	SSIM-L	8	8	16/16	100%
	EDGE	8	8	16/16	100%
	MSTLF-max	8	8	16/16	100%
	MSTLF-average	8	8	16/16	100%
	MSTLF-Frobenius	8	8	16/16	100%
	Total	64/64	64/64		
	%	100%	100%		

Supplementary Table 8: Wilcoxon signed rank test conducted on a per patient basis within *Dataset B* (LIDC/IDRI dataset, 8 patients in total) to assess the statistical significance of MSTLF-attention in comparison to other loss function configurations in CycleGAN. Each box shows the number of patients for whom MSTLF-attention is statistically better.

<i>Dataset B</i>					
UNIT		NIQE	PIQUE	Total	%
MSTLF-attention vs	Baseline	8	7	16/16	94%
	VGG-16	8	8	16/16	100%
	AE-CT	8	6	16/16	88%
	SSIM-L	8	5	16/16	81%
	EDGE	8	0	16/16	50%
	MSTLF-max	8	2	16/16	63%
	MSTLF-average	8	7	16/16	94%
	MSTLF-Frobenius	8	7	16/16	94%
	Total	64/64	42/64		
	%	100%	67%		

Supplementary Table 9: Wilcoxon signed rank test conducted on a per patient basis within *Dataset B* (LIDC/IDRI dataset, 8 patients in total) to assess the statistical significance of MSTLF-attention in comparison to other loss function configurations in UNIT. Each box shows the number of patients for whom MSTLF-attention is statistically better.

<i>Dataset C</i>					
Pix2Pix		NIQE	PIQUE	Total	%
MSTLF-attention vs	Baseline	44	31	75/100	75%
	VGG-16	47	24	71/100	71%
	AE-CT	21	12	33/100	33%
	SSIM-L	26	7	33/100	33%
	EDGE	50	38	88/100	88%
	MSTLF-max	43	27	70/100	70%
	MSTLF-average	36	16	52/100	52%
	MSTLF-Frobenius	26	18	44/100	44%
	Total	293/400	173/400		
	%	73%	43%		

Supplementary Table 10: Wilcoxon signed rank test conducted on a per patient basis within *Dataset C* (ELCAP dataset, 50 patients in total) to assess the statistical significance of MSTLF-attention in comparison to other loss function configurations in Pix2Pix. Each box shows the number of patients for whom MSTLF-attention is statistically better.

<i>Dataset C</i>					
cycleGAN		NIQE	PIQUE	Total	%
MSTLF-attention vs	Baseline	50	50	100/100	100%
	VGG-16	50	49	99/100	99%
	AE-CT	50	50	100/100	100%
	SSIM-L	50	50	100/100	100%
	EDGE	50	50	100/100	100%
	MSTLF-max	50	50	100/100	100%
	MSTLF-average	50	50	100/100	100%
	MSTLF-Frobenius	50	49	99/100	99%
	Total	400/400	398/400		
	%	100%	99%		

Supplementary Table 11: Wilcoxon signed rank test conducted on a per patient basis within *Dataset C* (ELCAP dataset, 50 patients in total) to assess the statistical significance of MSTLF-attention in comparison to other loss function configurations in CycleGAN. Each box shows the number of patients for whom MSTLF-attention is statistically better.

<i>Dataset C</i>					
UNIT		NIQE	PIQUE	Total	%
MSTLF-attention vs	Baseline	50	38	88/100	88%
	VGG-16	50	47	97/100	97%
	AE-CT	50	22	72/100	72%
	SSIM-L	50	12	62/100	62%
	EDGE	50	0	50/100	50%
	MSTLF-max	50	7	57/100	57%
	MSTLF-average	50	43	93/100	93%
	MSTLF-Frobenius	50	34	84/100	84%
	Total	400/400	203/400		
	%	100%	51%		

Supplementary Table 12: Wilcoxon signed rank test conducted on a per patient basis within *Dataset C* (ELCAP dataset, 50 patients in total) to assess the statistical significance of MSTLF-attention in comparison to other loss function configurations in UNIT. Each box shows the number of patients for whom MSTLF-attention is statistically better.